LASER MATERIALS AND TECHNOLOGY RESEARCH CENTER
OF GENERAL PHYSICS INSTITUTE

FINAL REPORT

CONTRACT F61775-99-WE024

Solid state Raman Materials Characterization and
Raman Shifting of 1.3 micron Laser Radiation

Moscow

June 2000

REPORT DOCUMENTATION PAGE

Form Approved OMB No. 0704-0188

1. REPORT DATE (DD-MM-YYYY) 27-06-2000	2. REPORT TYPE Final	3. DATES COVERED (FROM - TO) xx-xx-2000 to xx-xx-2000

4. TITLE AND SUBTITLE
Solid State Raman Materials Characterization And Raman Shifting Of 1.3 Micron Laser Radiation
Unclassified

5a. CONTRACT NUMBER
F61775-99-WE024

5b. GRANT NUMBER

5c. PROGRAM ELEMENT NUMBER

6. AUTHOR(S)
Basiev, Tasoltan T. ;

5d. PROJECT NUMBER

5e. TASK NUMBER

5f. WORK UNIT NUMBER

7. PERFORMING ORGANIZATION NAME AND ADDRESS
General Physics Institute of the Russian Academy of Sciences
38 Vavilov St
Moscow 117942, Russiaxxxxx

8. PERFORMING ORGANIZATION REPORT NUMBER

9. SPONSORING/MONITORING AGENCY NAME AND ADDRESS
EOARD
PSC 802 BOX 14
FPO, 09499-0200

10. SPONSOR/MONITOR'S ACRONYM(S)

11. SPONSOR/MONITOR'S REPORT NUMBER(S)

12. DISTRIBUTION/AVAILABILITY STATEMENT
APUBLIC RELEASE
,

13. SUPPLEMENTARY NOTES

14. ABSTRACT
This report results from a contract tasking General Physics Institute of the Russian Academy of Sciences as follows: The contractor will investigate experimentally the advantages and disadvantages of different solid state Raman materials with respect to their use for high average power lasers, especially the iodine laser at 1.3 microns.

15. SUBJECT TERMS
EOARD; Raman laser materials

16. SECURITY CLASSIFICATION OF:			17. LIMITATION OF ABSTRACT Public Release	18. NUMBER OF PAGES 89	19. NAME OF RESPONSIBLE PERSON Fenster, Lynn lfenster@dtic.mil
a. REPORT Unclassified	b. ABSTRACT Unclassified	c. THIS PAGE Unclassified			19b. TELEPHONE NUMBER International Area Code Area Code Telephone Number 703767-9007 DSN 427-9007

Standard Form 298 (Rev. 8-98)
Prescribed by ANSI Std Z39.18

REPORT DOCUMENTATION PAGE

1. AGENCY USE ONLY (Leave blank)	2. REPORT DATE	3. REPORT TYPE AND DATES COVERED
	27-June-2000	Final Report

4. TITLE AND SUBTITLE

Solid State Raman Materials Characterization And Raman Shifting Of 1.3 Micron Laser Radiation

5. FUNDING NUMBERS

F61775-99-WE024

6. AUTHOR(S)

Professor Tasoltan Tazretovich Basiev

7. PERFORMING ORGANIZATION NAME(S) AND ADDRESS(ES)

General Physics Institute of the Russian Academy of Sciences
38 Vavilov St
Moscow 117942
Russia

8. PERFORMING ORGANIZATION REPORT NUMBER

N/A

9. SPONSORING/MONITORING AGENCY NAME(S) AND ADDRESS(ES)

EOARD
PSC 802 BOX 14
FPO 09499-0200

10. SPONSORING/MONITORING AGENCY REPORT NUMBER

SPC 99-4024

11. SUPPLEMENTARY NOTES

12a. DISTRIBUTION/AVAILABILITY STATEMENT

Approved for public release; distribution is unlimited.

12b. DISTRIBUTION CODE

A

13. ABSTRACT (Maximum 200 words)

This report results from a contract tasking General Physics Institute of the Russian Academy of Sciences as follows: The contractor will investigate experimentally the advantages and disadvantages of different solid state Raman materials with respect to their use for high average power lasers, especially the iodine laser at 1.3 microns.

14. SUBJECT TERMS

EOARD, Raman laser materials

15. NUMBER OF PAGES

87

16. PRICE CODE

N/A

17. SECURITY CLASSIFICATION OF REPORT	18. SECURITY CLASSIFICATION OF THIS PAGE	19, SECURITY CLASSIFICATION OF ABSTRACT	20. LIMITATION OF ABSTRACT
UNCLASSIFIED	UNCLASSIFIED	UNCLASSIFIED	UL

CONTENT

1. Introduction

Stimulated Raman Scattering (SRS) as a nonlinear process was discovered in 1962 at the beginning of the laser era [1.1]. Now application of solid-state Raman materials for stimulated Raman scattering (SRS) is one of the most perspective ways to develop high-gain reliable and small-size devices for shifting laser radiation frequency.

Raman scattering is the nonlinear optical phenomena based on two photon transition resonant to the frequency of the internal crystal phonons or quasimolecular vibrations determined by the crystal chemical composition, crystallographic structure, symmetry and parameters of the lattice. The frequency of the most intense Raman phonon ν_R determines the SRS frequency shift ($\nu_{stokes} = \nu_{pump} - \nu_R$) that usually varies from 100 to about 1300 cm^{-1} for solid state materials. In comparison with second order processes (harmonic generation and optical parametric oscillation), SRS is the third order nonlinear process. Hence, it does not require phase matching conditions to obtain high conversion efficiency. That is why there is no limitation for the light to crystal interaction length, which can be from few mm up to some tens of meters.

In our recent investigations barium nitrate $Ba(NO_3)_2$ and $KGd(WO_4)_2$ tungstate crystal (KGW) were found to be very promising nonlinear media for SRS [1.2-1.7]. They possess strong symmetrical Raman active phonon modes with 1047 cm^{-1}, 901 cm^{-1} and 767 cm^{-1} frequencies, respectively. At room temperature the linewidth of this mode in $Ba(NO_3)_2$ was measured to be extremely narrow, 0.4 cm^{-1} that is much less than that for other solid state Raman materials [1.8, 1.9]. This results in a very high value of Raman gain coefficient and the best performance of $Ba(NO_3)_2$ for frequency shift of nanosecond laser radiation with narrow spectral width. KGW crystal shows less peak value of Raman gain cross section, but 5 times higher integral Raman cross section which is very important for Raman frequency conversion of picosecond laser pulses with a wide spectrum of oscillation. At the same time KGW crystal

possess much better moisture resistance, hardness and thermoconductivity characteristics that are very important for high power laser frequency converter development.

Our preliminary analysis allows us to select a number of insulators (diamond, BeO, MgO, Al_2O_3, Y_2O_3 etc.) and semiconductors (SiC, AlN, BN, Si, GaP, AlSb, InP, GaAs, ZnO, GaSb, ZnS) with a very high thermoconductivity as potential candidates for high average power Raman active media. But there is not systematic comparative study of Raman frequency, line broadening, and Raman scattering peak and integral cross-sections, as well as Raman gain in literature. Our first experimental estimations show that these parameters differ considerably from a crystal to crystal. For example, Y_2O_3 crystal has 22 times higher Raman scattering cross-section than that for Al_2O_3 with the same thermoconductivity.

The possibility to design an efficient solid-state Raman shifter for 1.06 and 1.3 μm neodymium pump lasers with repetition rate up to 50 Hz was demonstrated in [1.4-1.7]. It was shown that Raman converter could be designed as a single pass oscillator and amplifier unit. It can be composed as a separate laser unit, including Raman crystal placed in the additional optimized optical cavity for increasing the length of light to crystal interaction that results in threshold decrease and increase of light to light conversion efficiency. There can be an intracavity configuration with the nonlinear crystal installed inside the pump laser cavity. These three different configurations exhibit features, common for laser devices, such as low divergence, high spatial brightness and narrow spectral line width and high conversion efficiency.

References to chapter 1:

1.1.   E.J.Woodbury, Ng W.K., Proc. IRE, **50**, 2347 (1962).

1.2.   T.T.Basiev, V.N.Voitsekhovskii, P.G.Zverev, et al. Sov. J. Quantum Electron., **17,** 1560 (1987).

1.3.   P.G.Zverev, Y.T.Murray, et al. Optics Communications, **97,** 59 (1993).

1.4.   P.G.Zverev, T.T.Basiev. 3rd International Conference Laser M2P, Lyon, France, Dec. 1993 in J. de Physique, **4,** C4-599 (1994).

1.5.   P.G.Zverev, T.T.Basiev, A.M.Prokhorov. CLEO/Europe'94, Amsterdam, The Netherlands, in Technical Digest, paper CWF74.

1.6.   P.G.Zverev, T.T.Basiev, I.V.Ermakov, et al . SPIE-The International Society for Optical Engineering, **2498,** 164-170 (1994).

1.7.   P.G.Zverev, T.T.Basiev, OSA Proceedings on Advanced Solid State Lasers, **24,** 288 (1995).

1.8.   P.G.Zverev, T.T.Basiev, Quantum Electronics, **25,** 1204 (1995).

1.9.   P.G.Zverev, T.T.Basiev, et al. OSA Trends in Optics and Photonics on Advanced Solid State Lasers, Washington, DC, Ed.S.Payne and C.R.Pollock, 1, 554-559 (1996).

2. Spontaneous Raman spectroscopy of tungstate and molybdate crystals for Raman lasers

Stimulated Raman scattering (SRS) is a new promising technique for shifting laser radiation frequency to new spectral regions. The efficiency of nonlinear crystal depends on spectroscopic parameters of the SRS-active mode, i.e. peak and integral Raman scattering cross-sections and linewidth. Previous results on spontaneous Raman spectroscopic study [2.1, 2.2] have revealed the essential advantages of the series of tungstate and molybdate single crystals with isolated $[WO_4]$ and $[MoO_4]$ groups for Raman lasers. They exhibit intensive lines in Raman spectra which correspond to symmetrical vibration in $[WO_4]$ and $[MoO_4]$ molecular ionic groups.

Up to now the most efficient and widely used SRS material is $Ba(NO_3)_2$ crystal. It has the highest peak Raman scattering cross section due to the narrowest SRS-active A_g mode ($\Delta\nu_R = 0.4$ cm^{-1}) [2.3]. Among tungstate and molybdate crystals the narrowest linewidth ($\Delta\nu_R$) is observed in $BaWO_4$ and $BaMoO_4$ crystals and is approximately 3 times broader than that in $Ba(NO_3)_2$. Due to a 2.5÷3 times larger integral Raman scattering cross section, these materials exhibit approximately the same values of the peak cross section as that observed in $Ba(NO_3)_2$ crystal [2.2]. Other tungstate and molybdate crystals reveal approximately the same values of the integral Raman scattering cross section, while $\Delta\nu_R$ value is essentially increased in the series of tungstates (MeWO$_4$) and molybdates (MeMoO$_4$) with changing the Me^{2+} cation from Ba to Sr and Ca from 1.6 to 6 cm^{-1} at 300K. The aim of this chapter was to investigate the correlation of the linewidth value ($\Delta\nu_R$) with the peculiarities in spontaneous Raman spectra of tungstates and molybdates with sheelite structure.

2.1. The objects and techniques for investigation

Spontaneous Raman spectra of tungstates MeWO$_4$ and molybdates MeMoO$_4$ (Me = Ca, Sr, Ba, Pb, Zn) were investigated in our experiments. Most of the samples were grown by

Czochralski technique as bulk single crystals. They were oriented by an X-ray technique and cut along and perpendicular to the c-axis. Polarized spontaneous Raman spectra were measured for these single crystals. The $PbWO_4$, $PbMoO_4$, $SrWO_4$, $ZnWO_4$ and $ZnMoO_4$ were prepared as polycrystalline samples by heating the mixture of WO_3 with appropriate carbonate $MeCO_3$ to the temperature 1100÷1200 °C for about 30÷40 hours.

Raman spectra were investigated with a «SPEX Ramalog-1403» spectrometer at 77 K and 300 K using a conventional scattering technique under Ar-laser (488 nm) excitation. High temperature Raman spectra up to 1920 K were registered using an original technique described in Ref. [2.4]. It utilized excitation by pulsed periodic (f=10 kHz) Cu vapor laser ($\lambda = 501.5$ nm). The registration of spontaneous Raman spectra with the time-strobe technique provided a high signal to thermal radiation background ratio. High temperature Raman spectra allowed us to study the variation of the Raman linewidth ($\Delta\nu_R$) and frequency shift versus the temperature up to the melting point and to investigate phase transformation in tungstate and molybdate series.

2.2. The vibrational spectra of tungstate and molybdate crystals with isolated WO₄ and MoO₄ complexes

Spontaneous Raman spectra of calcium, strontium and lead tungstates and molybdates were studied extensively in the mid 60's [2.5-2.9]. To our knowledge the detailed Raman and IR spectroscopic investigations of $BaWO_4$ and $BaMoO_4$ crystals are still absent. All substances under study, excluding $ZnWO_4$ and $ZnMoO_4$, have a sheelite crystal structure with tetragonal symmetry C_{4h}^6 at room temperature. The primitive cell includes two formula units. The molecular ionic group of $[WO_4]^{2-}$ or $[MoO_4]^{2-}$ with strong covalent bonds W-O or Mo-O is the peculiarity of the sheelite structure. Due to weak coupling between the ionic group and the Me^{2+} cation, the vibrational modes in spontaneous Raman spectra of sheelite crystals can be

divided into two groups, internal and external. The internal vibrons correspond to the oscillations inside $[WO_4]^{2-}$ or $[MoO_4]^{2-}$ molecular group with an immovable mass center. The external or lattice phonons correspond to the motion of the Me^{2+} cation and the rigid molecular unit.

According to Ref. [2.5] the $[WO_4]^{2-}$ or $[MoO_4]^{2-}$ tetrahedrons in a free space have T_d - symmetry. From factor group analysis it follows that $3N=15$ degrees of freedom for $[WO_4]^{2-}$ or $[MoO_4]^{2-}$ free molecular ions can be divided into four internal modes denoted by $\nu_1(A_1)$, $\nu_2(E)$, $\nu_3(F_2)$ and $\nu_4(F_2)$, one free rotation mode - $\nu_{f.r.}(F_1)$ and one translation mode (F_2). When a $[WO_4]^{2-}$ or a $[MoO_4]^{2-}$ ion is placed into the sheelite structure its point symmetry is reduced to S_4. This results in the splitting of all degenerate vibrations due to the Crystal Field (CF) effect [2.5]. Moreover the presence of two molecular groups in the primitive cell further alters the structure of vibrational modes due to Davydov Splitting (DS). For example the splitting of $\nu_1(A_1)$ and $\nu_3(F_2)$ modes of a free molecule in the sheelite structure will be as follows:

$$\nu_1(A_1) \quad \xrightarrow{CF} \quad \nu_1(A) \quad \xrightarrow{DS} \quad \nu_1(A_g) + \nu_1(B_u) \tag{2.1a}$$

$$\nu_3(F_2) \quad \xrightarrow{CF} \quad \nu_3(E) + \nu_3(B) \quad \xrightarrow{DS} \quad \nu_3(E_g) + \nu_3(E_u) + \nu_3(B_g) + \nu_3(A_u) \tag{2.1b}$$

Group theory calculation shows 26 different vibrations:

$$\Gamma = 3A_g + 5A_u + 5B_g + 3B_u + 5E_g + 5E_u \tag{2.2}$$

for K=0 wavevector in the sheelite primitive cell. All even vibrations (A_g, B_g and E_g) are Raman-active, while odd modes ($4A_u$ and $4E_u$) can be registered only in the infrared spectra. Three B_u vibrations are silent modes. The system (2) includes also one A_u and one E_u acoustic vibrations.

Table 2.1. Raman mode frequencies in BaWO$_4$ and BaMoO$_4$ single crystals at 300 K, at temperatures about ($\beta \rightarrow \alpha$) phase transition (BaMoO$_4$) and at the melting point.

Lattice mode symmetry C$_{4h}^6$	BaWO$_4$			BaMoO$_4$					ASSIGNMENTS
	300 K (solid) C$_{4h}^6$	1800 K (solid) C$_{4h}^6$	1820 K (melt)	300 K (solid) C$_{4h}^6$	1600 K (solid) (before P.T.) C$_{4h}^6$ (β)	1605 K (solid) (after P.T.) cubic (α)	1770 K (solid) cubic (α)	1800 K (melt)	
A$_g$	925	910	909	892	878	877	873	872	$\nu_1(A_1)$
B$_g$	831	816	804	837	825	802	794	777	$\nu_3(F_2)$
E$_g$	795	775		791	771				
E$_g$	353	338	370	358	347	359	356	356	$\nu_4(F_2)$
B$_g$	345	-		345					
B$_g$	332	318	326	324	313	313	313	314	$\nu_2(E)$
A$_g$	332			324					
E$_g$	191	109	-	188	143	134	-	-	$\nu_{f.r.}(F_1)$
A$_g$	150			140					free rotation
B$_g$	132	-	-	137	-	-	-	-	$\nu_{ext.}$ - external
E$_g$	101	73	-	110	-	-	-	-	modes
E$_g$	75	-	-	74	57	45	-	-	WO_4^{2-}, MoO_4^{2-}, and
B$_g$	63	58	-	76	73	-	-	-	Ba^{2+} motions

Spontaneous Raman spectra registered in our experiments correlate well with earlier results published in Ref. [2.5-2.9]. At room and higher temperatures spontaneous Raman spectra of new $BaWO_4$ and $BaMoO_4$ crystals with factor group assignments of the Raman-active modes are presented in Figs. 2.1 and 2.2 and detailed in Table 2.1. $BaWO_4$ and $BaMoO_4$ crystals have similar sheelite crystallographic structure at 300 K and higher temperatures.

The phase transition from tetragonal sheelite (β) to cubic structure (α) was discovered in $BaMoO_4$ at 1600 K. One can see the merging of two ν_3 lines and the shift of ν_{ext} mode in the Raman spectra of $BaMoO_4$ at temperatures above 1600 K (Fig.2.2). From Eq. (2.1b) it follows that the splitting of the $\nu_3(F_2)$ vibration into two $\nu_3(E_g)$ and $\nu_3(B_g)$ components is a result of the CF splitting when the cubic point symmetry T_d of a free $[MoO_4]^{2-}$ anion is reduced to tetragonal S_4. Merging of $\nu_3(E)$ and $\nu_3(B)$ components in the Raman spectra at high temperature proves the increase of the point symmetry of the $[MoO_4]^{2-}$ unit to the cubic symmetry at $\beta \rightarrow \alpha$ transformation. Thus, the symmetry of the $[MoO_4]^{2-}$ molecular anion in α-phase is similar to that of a free $[MoO_4]^{2-}$ tetrahedron in the melt. If one considers the correlation rules between the site point and lattice space group symmetry [2.10], the $\beta \rightarrow \alpha$ transformation results in the formation of cubic structure for α - phase.

Experiments on heating and cooling the $BaMoO_4$ crystal revealed that the above mentioned $\beta \leftrightarrow \alpha$ phase transition was reversible. It was impossible to stabilize $BaMoO_4$ crystal in α-phase at 300 K even by quick quenching technique. The presence of this phase transition results in difficulties with growing $BaMoO_4$ single crystals from melt. Nevertheless it was possible to synthesize transparent $BaMoO_4$ single crystals with β (sheelite) structure by Czochralsky technique.

The change of Raman-active mode frequencies with changing the sort of Me^{2+} cation (Ca^{2+}, Sr^{2+}, Ba^{2+} and Pb^{2+}) in the series of tungstate ($MeWO_4$) and molybdate ($MeMoO_4$) crystals was investigated in our experiments and is presented in Figs. 2.3 and 2.4. From these Figs. it

follows that the variations of vibrational level energies are similar for both tungstate and molybdate series.

There can be various reasons of vibrational energy shifts for different Me^{2+} cations. Kanamori et al. [2.9] have proposed the predominant influence of the cation mass on the frequencies of lower lying external vibrations ($2B_g + 2E_g$).
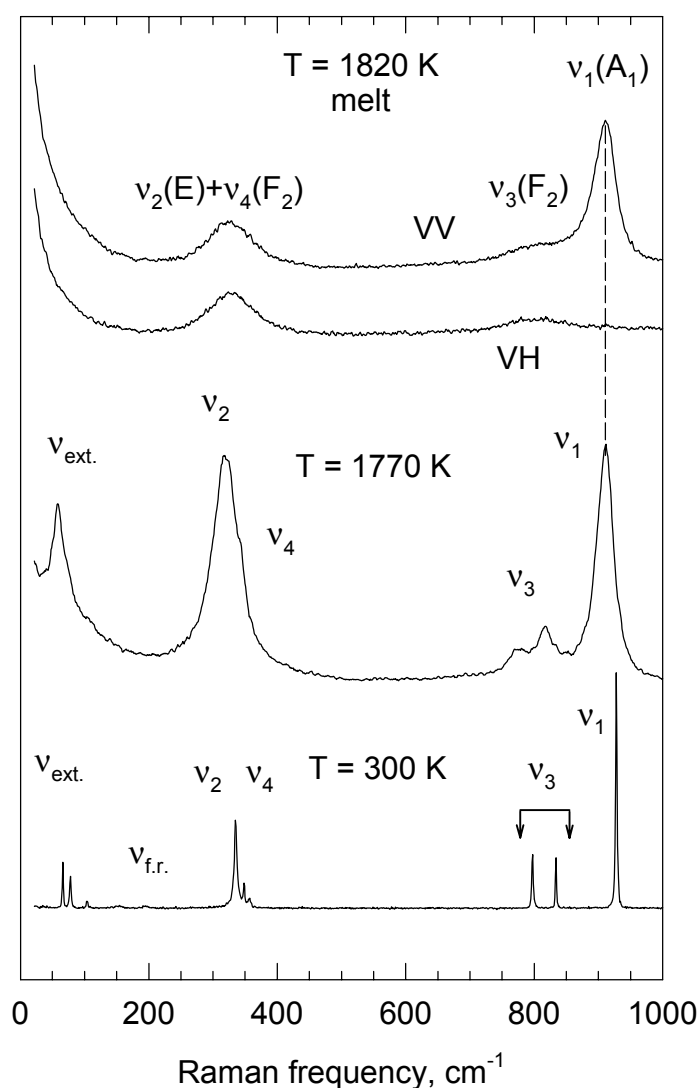
Fig. 2.1. Unpolarized spontaneous Raman spectra of BaWO$_4$ crystal and polarized spectra of the melt at different temperatures (VV – parallel excitation and registration polarization, VH - perpendicular).
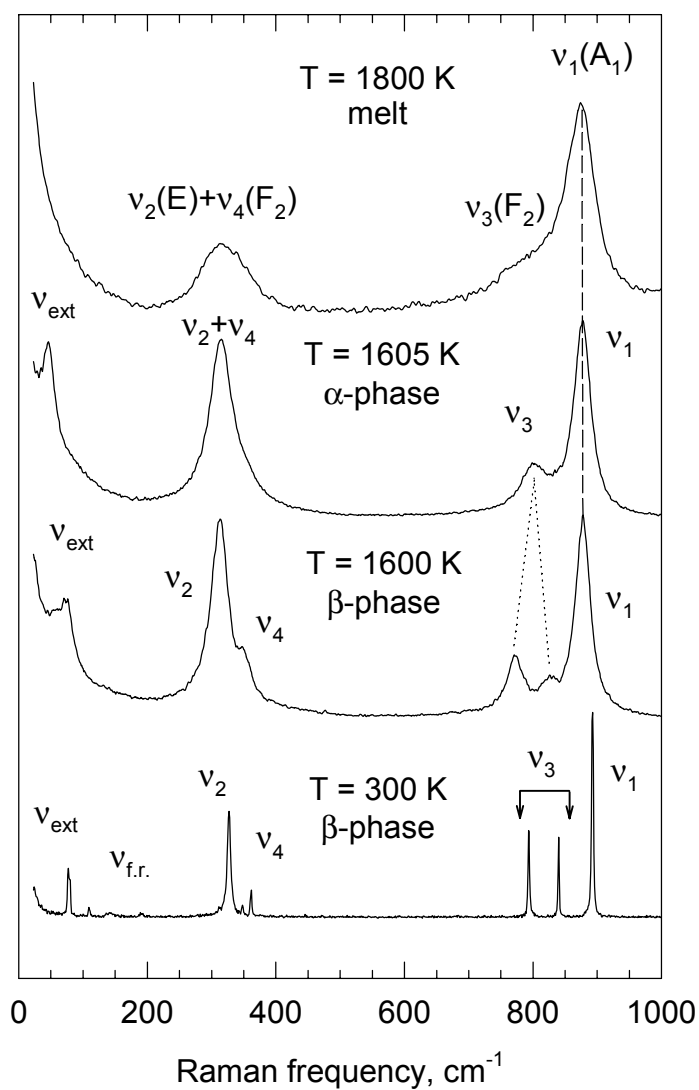
Fig. 2.2. Unpolarized spontaneous Raman spectra of BaMoO$_4$ crystal in crystalline and molten states at different temperatures.
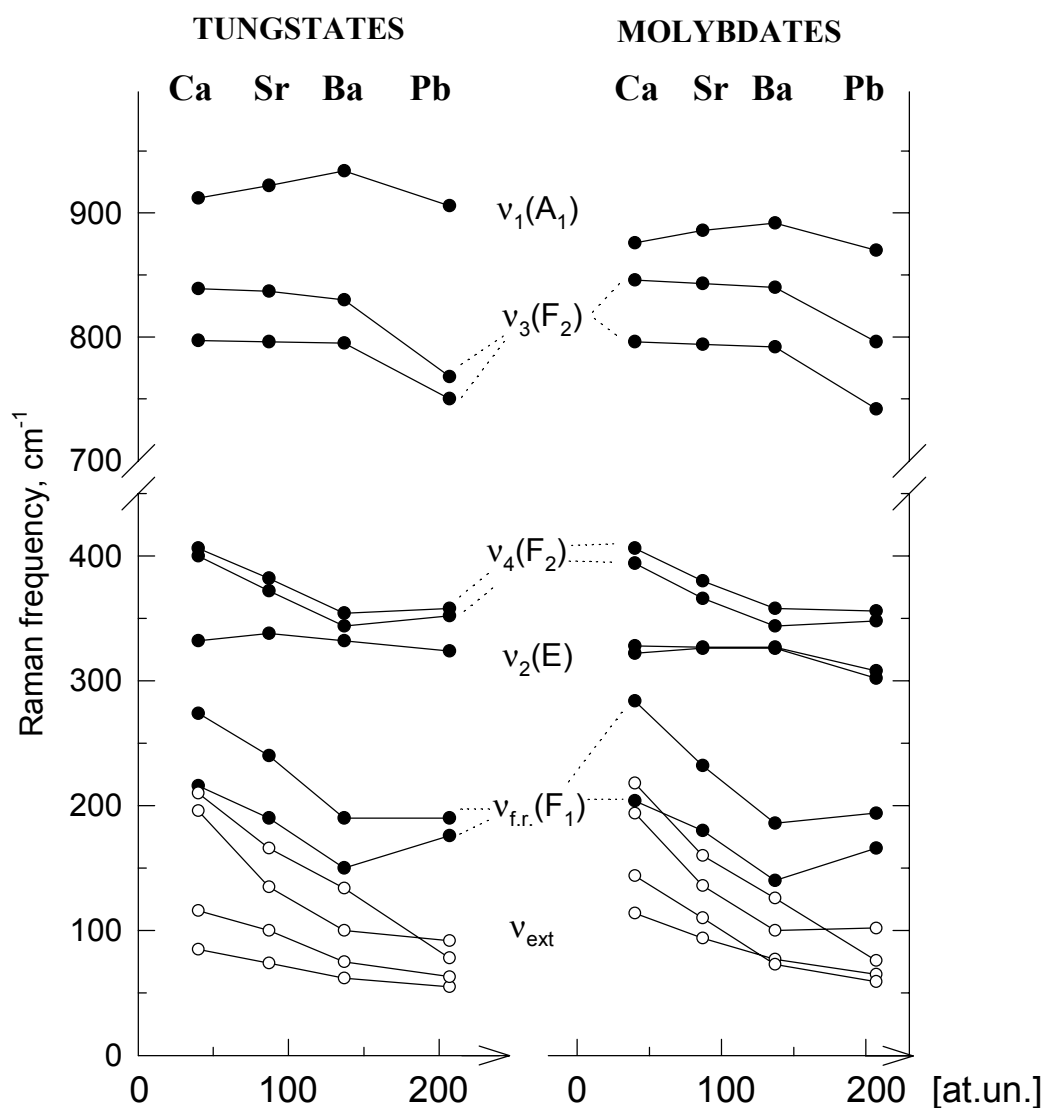
Fig. 2.3. Frequency shifts of Raman-active modes in tungstate (*MeWO₄*) and molybdate (*MeMoO₄*) crystals with increasing a mass of Me^{2+} cation in the range Ca → Sr → Ba → Pb at 300 K. Filled dots – internal vibrons, hollow dots – lattice, external phonons.

Fig. 2.4. Frequency shifts of Raman-active internal modes in tungstate (*MeWO₄*)

and molybdate (*MeMoO₄*) crystals with increasing lattice constant **c** [Å] in the

range Ca → Sr → Pb → Ba at 300 K.

This is in good agreement with monotonous decrease of these mode frequencies with growing the mass of Me^{2+} cation in the series ($Ca^{2+} \rightarrow Sr^{2+} \rightarrow Ba^{2+} \rightarrow Pb^{2+}$) registered in our experiments (Fig.2.3).

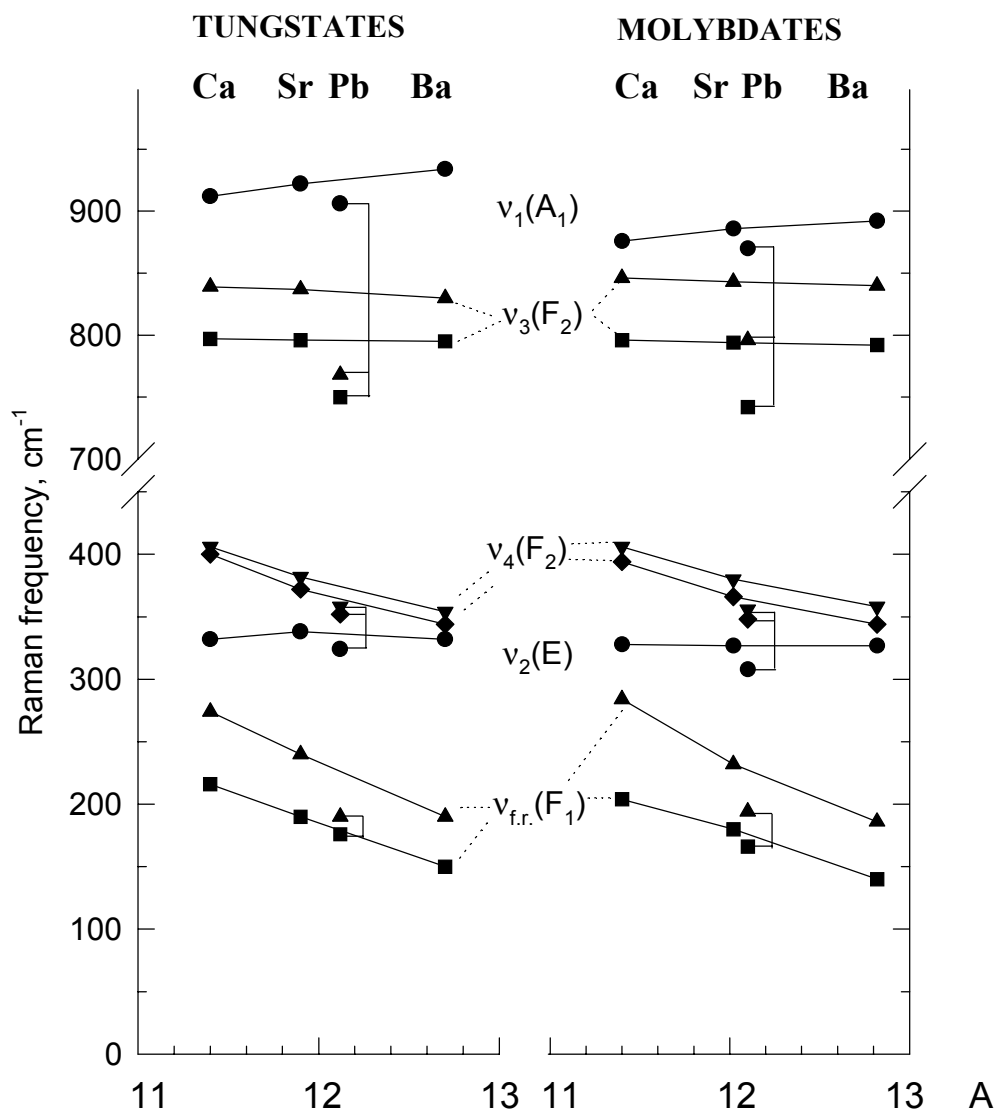In the first approximation of the internal–external mode model, the effect of the cation type on the internal mode frequencies $\{\nu_1(A_1),\ \nu_2(E),\ \nu_3(F_2),\ \nu_4(F_2),\ \nu_{f.r.}(F_1)\}$ is neglected and frequency values should be constant. Our experiments showed (Fig. 2.3) that the frequency of only one $\nu_2(E)$ doublet mode is not shifted with moving along the sheelite series. However other internal mode frequencies are considerably shifted with changing the cation type (Fig. 2.3, 2.4).

There are several reasons that can be responsible for this phenomenon. The growth of the cation size increases the cell parameters and, consequently, the interionic distance including the W-O or Mo-O distance inside $[WO_4]^{2-}$ or $[MoO_4]^{2-}$ complexes (Table 2.2). In turns, force constants for some internal vibrational modes in these anions can decrease in cation series $Ca \rightarrow Sr \rightarrow Ba$. Probably the influence of the unit cell parameters on the force constants is predominant only for $\nu_4(F_2)$ and $\nu_{f.r.}(F_1)$ vibrational modes(Fig. 2.4). The unit cell parameters for $PbWO_4$ and $PbMoO_4$ are close to those of $SrWO_4$ and $SrMoO_4$ (Table 2.2). So we could expect that the frequency values of internal vibrations in lead sheelites would be close to those in strontium. However, contrary to this, our data displayed essential hops down for all internal mode frequencies in $PbWO_4$ and $PbMoO_4$ compared with other sheelites (Fig. 2.4). Larger shifts were observed for higher lying $\nu_1 (A_g)$ and $\nu_3 (B_g)$, $\nu_3 (E_g)$. It is impossible to explain this phenomenon only due to the peculiarities of the unit cell of Pb –sheelites.

Table 2.2. Integral and peak Raman scattering cross sections, linewidths at 77 and 300 K of the SRS-active ν_1 (A_g) mode in Ba(NO$_3$)$_2$, *Me*WO$_4$ and *Me*MoO$_4$ (*Me* = Ba, Sr, Ca, Pb) crystals versus physical properties of Me^{2+} cation, lattice parameters and energy splitting of ν_1 vibration (ΔE).

Crystal	Raman frequency ν_R (300K) cm^{-1}	Integral cross section, Σ_{int}* [a. u.]	Peak cross section, Σ_{peak}* [a. u.]	Linewidth $\Delta\nu_R$, [cm^{-1}] 300 K	Linewidth $\Delta\nu_R$, [cm^{-1}] 77 K	Atomic mass of M^{2+} cation [at. un.]	Ionic radius of M^{2+} cation [Å]	Electro-negativity of M^{2+} cation [11]	Lattice parameters [12] [Å] c	Lattice parameters [12] [Å] a	ΔE*** cm^{-1}	W-W and Mo-Mo distance in the lattice Å
Ba(NO$_3$)$_2$	1048	21	63	0.4	0.3	137.34	1.42	0.78	8.11	8.11	< 0.65*****	–
BaWO$_4$	925	52	64	1.6	0.97	137.34	1.42	0.78	12.720	5.640	0÷1	6.95
SrWO$_4$	921	-	-	3.0	1.45	87.62	1.25	1.06	11.921	5.417	28	6.5
CaWO$_4$	911	50	18.4	5.6 (6.9**)	3.1 (3.7**)	40.08	1.12	1.22	11.376	5.242	58	6.26
PbWO$_4$	905	-	-	4.7	1.87	207.19	1.29	3.08	12.12	5.50	32	6.65
ZnWO$_4$****	908	-	-	8.0	5.0	65.38	0.9	2.98	-	-	-	-
BaMoO$_4$	892	55	62	1.85	1.1	137.34	1.42	0.78	12.82	5.62	0÷1	7.0
SrMoO$_4$	887	63	51	2.5	1.2	87.62	1.25	1.06	12.02	5.394	22	6.58
CaMoO$_4$	879	65	34	5.5	2.3	40.08	1.12	1.22	11.43	5.266	52	6.28
PbMoO$_4$	871	-	-	8.0**	3.2**	207.19	1.29	2.98	12.108	5.436	36	6.63
ZnMoO$_4$****	971	-	-	4.5	-	65.38	0.9	2.98	-	-	-	-

*- integral and peak cross sections are normalized values [2.2].

**- total linewidth of inhomogeneously broadened mode.

*** - this value was determined according to the method described below in the text.

**** - ZnWO$_4$ and ZnMoO$_4$ crystals has different from sheelite crystallographic structure.

***** - this value was estimated from A$_1$ mode splitting in Ba(NO$_3$)

We proposed that there should be another predominant factor in this case, namely the partially covalent bond between the Me^{2+} cation and oxygen atoms in $[WO_4]^{2-}$ or $[MoO_4]^{2-}$ complexes. According to Ref. [2.13] this factor influences the force constants of internal vibrations. The higher value of electronegativity (lower basicity) of Me^{2+} cation correlates with the higher force constant of the stretching vibration in tetrahedral group and higher frequencies of vibration modes (Fig. 2.5).

The formation of a Me^{2+}-O partially covalent bond also has to change the efficient mass of the oscillating atomic groups. The reduced mass of the metal–oxygen pair should be considered instead of oxygen atomic mass in this case. Thus, the Me^{2+} cation mass can indirectly influence the internal vibration frequencies of $[WO_4]^{2-}$ and $[MoO_4]^{2-}$ anions.

According to Ref. [2.13] the effect of Me^{2+} cation on internal vibration frequencies mainly occurred through the force constants than through the reduced mass of the Me^{2+}-O pair. However, Lasarev et al. [2.13] did not consider the case of a very large cation mass such as Pb^{2+}.

In this connection the investigation of the influence of different types of Me^{2+} cation on the internal vibrational modes is of great interest. It is difficult to study this phenomenon for crystalline state as the static crystal field and the dynamic interaction can strongly disguise Me^{2+}-cations effect on anion internal vibrations. These crystal lattice effects are absent in a molten state and spontaneous Raman spectra of melts can give the information on the vibrational level schemes of unperturbed $[WO_4]^{2-}$ and $[MoO_4]^{2-}$ complexes with the definite Me^{2+} cation environment. Our spectroscopic experiments of molten tungstates and molybdates were carried out utilizing the high temperature Raman spectroscopic technique [2.4].

The observed Raman spectra of molten sheelites were typical to tetrahedron anions with T_d symmetry (Figs. 2.1, 2.2, 2.6). Four vibrational modes $\nu_1(A_1)$, $\nu_2(E)$, $\nu_3(F_2)$ and $\nu_4(F_2)$ were registered in the Raman spectra of the melts. The $\nu_1(A_1)$ mode was totally polarized in VH

geometry in these spectra which is characteristic for totally symmetric stretching oscillation of tetrahedron complexes.

In addition to sheelites the molten $ZnWO_4$ and $ZnMoO_4$ crystals were spectroscopically investigated in order to trace the effect of the mass reduction on internal vibrational modes of $[WO_4]^{2-}$ and $[MoO_4]^{2+}$ complexes. An electronegativity of Zn^{2+} cation approximately equals that of Pb^{2+} while the mass of Pb^{2+} cation exceeds the mass of Zn^{2+} and other investigated cations.

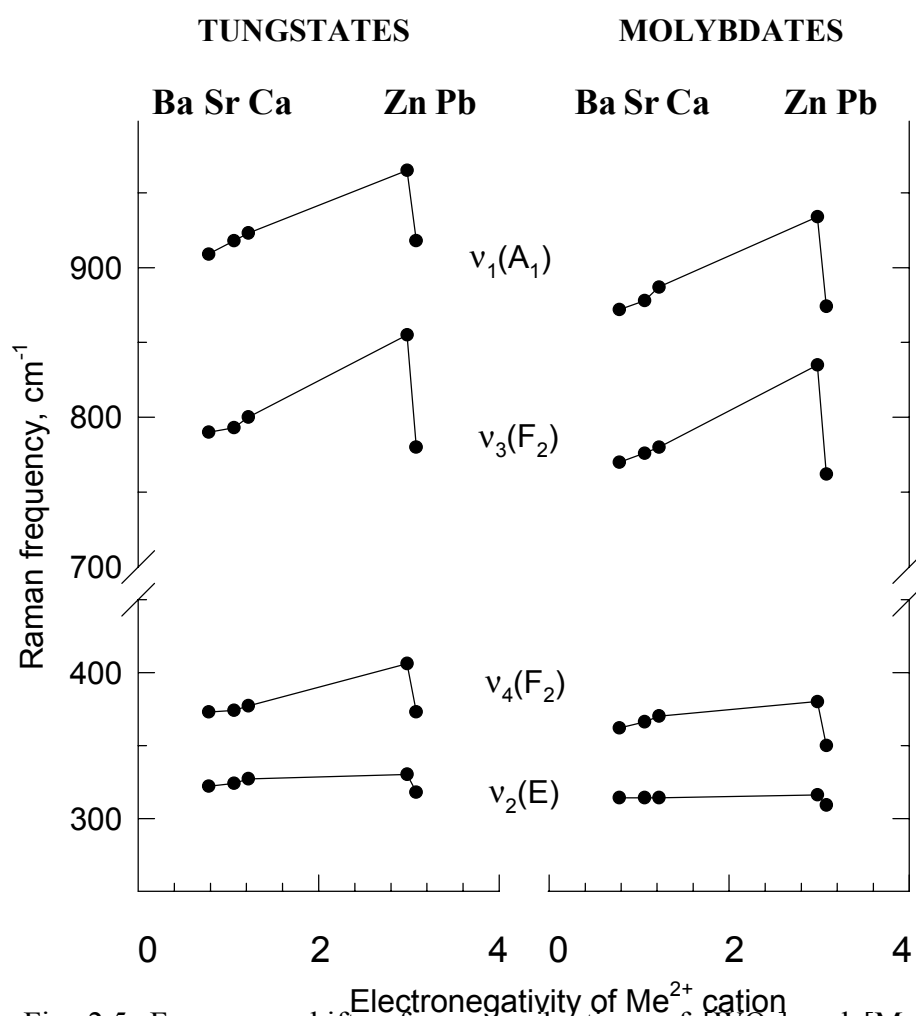Fig. 2.5. Frequency shifts of $v_1 \div v_4$ vibrations of $[WO_4]$ and $[MoO_4]$ units in MeWO$_4$ and MeMoO$_4$ melts versus the electronegativity of Me^{2+} cations in the range Ba $\rightarrow$ Sr $\rightarrow$ Ca $\rightarrow$ Zn $\rightarrow$ Pb.

In crystalline state $ZnWO_4$ and $ZnMoO_4$ exhibit other than sheelite crystal structure. The tungsten has an octahedral oxygen environment in a wolframite type of $ZnWO_4$ [2.12]. Our experimental high temperature Raman spectra reliably show that the octahedral complexes are transformed into $[WO_4]^{2-}$ tetrahedrons in $ZnWO_4$ melt (Fig. 2.7). A similar tetrahedron construction of the $[MoO_4]^{2-}$ anion is observed in molten $ZnMoO_4$. Thus, the Raman spectra of $ZnWO_4$ and $ZnMoO_4$ melts could also be used to study the effect of mass and electronegativity of Me^{2+} cation on vibration spectra in the series of tungstate and molybdate melts.

Fig. 2.5 presents the $\nu_1(A_1)$, $\nu_2(E)$, $\nu_3(F_2)$, $\nu_4(F_2)$ mode frequencies versus the electronegativity of Me^{2+} cation for Raman spectra of molten tungstates and molybdates. This figure shows that the growth of electronegativity (the reduce of basicity) of Me^{2+} cation results in the increase of $\nu_1(A_1)$, $\nu_3(F_2)$ and $\nu_4(F_2)$ mode frequencies in tungstate and molybdate melts in the series Ba→Sr→Ca→Zn. These data support the predominant influence of the basicity of Me^{2+} - cations on the force constants of vibration in these molecular complexes. The effect of the change of reduced mass of Me^{2+}-O pair on this regularity is small. However, the reduced mass effect is considerable for $PbWO_4$ and $PbMoO_4$. Essential hops down of the vibrational frequencies of $[WO_4]^{2-}$ and $[MoO_4]^{2-}$ complexes were registered in the Raman spectra of $PbWO_4$ and $PbMoO_4$ melts. This shows that the effect of Pb^{2+} electronegativity growth on vibrational level frequencies of $[WO_4]^{2-}$ and $[MoO_4]^{2-}$ complexes can be compensated by increasing the reduced mass of Pb-O pair.

These results show that the effect of the peculiarities of Me^{2+} -cation type (electronegativity and a mass) on the variation of vibration energy diagrams of unperturbed tetrahedron molecule have to be taken into account in the analysis of internal vibrational modes in sheelite crystals. This effect was not considered in the previous Refs. [2.6, 2.7], where vibrational level diagrams of the $[WO_4]^{2-}$ or $[MoO_4]^2$ – anions in the water solutions were supposed as those of unperturbed anions.

Fig. 2.6. Unpolarized spectra of CaWO$_4$ crystal and polarized spectra of the melt at different temperatures (VV – parallel excitation and registration polarization, VH - perpendicular).

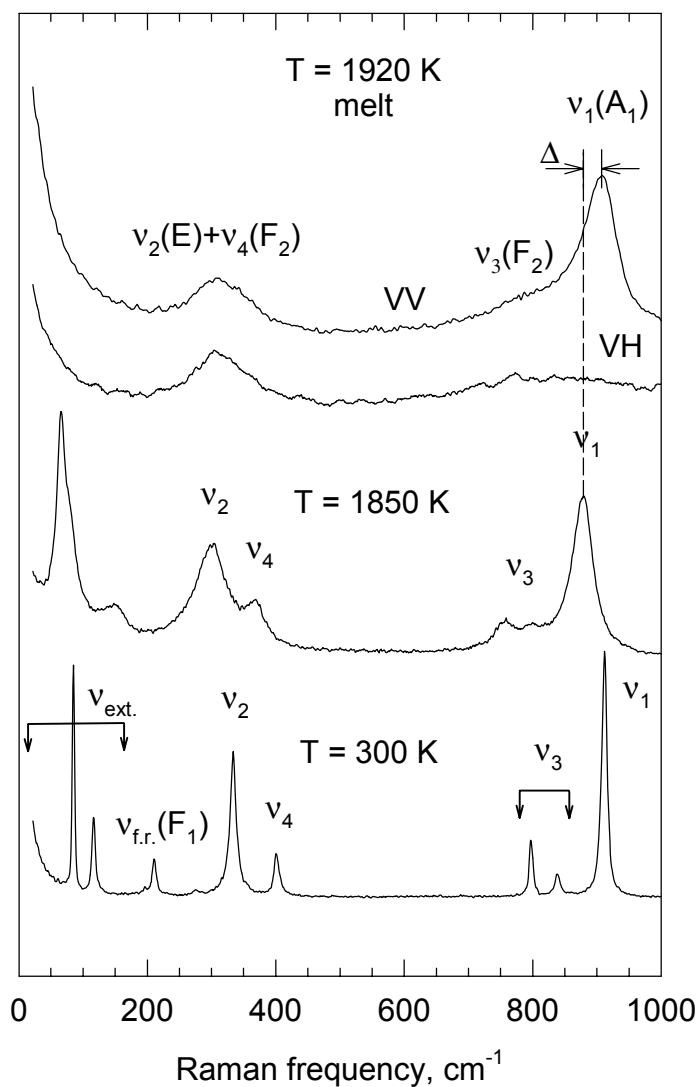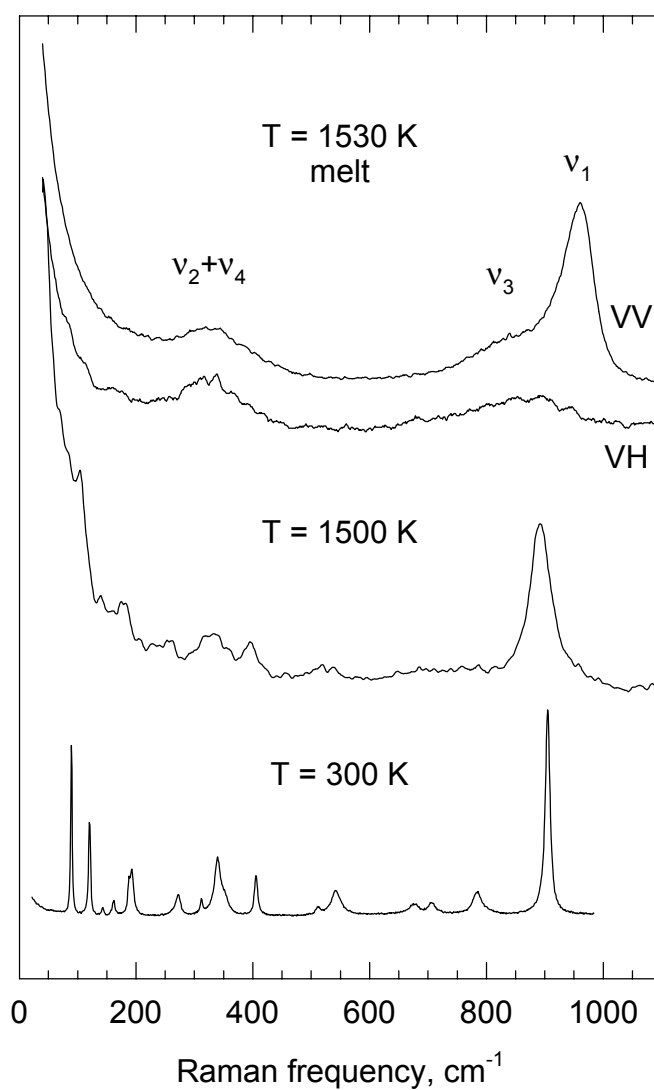Fig. 2.7. Unpolarized spectra of $ZnWO_4$ crystal and polarized spectra of the melt at different temperatures (VV – parallel excitation and registration polarization, VH - perpendicular).

Hops down of the frequencies of tetrahedron vibrations in the Raman spectra of $PbWO_4$ and $PbMoO_4$ for melts (Fig. 2.5) correlate with similar hops for crystalline series (Figs.2.3, 2.4). Thus, the effect of Me^{2+}-cation mass on vibrational energy level diagrams of $[WO_4]^{2-}$ or $[MoO_4]^{2-}$ – anions both in molten and in crystalline states are predominant for $PbWO_4$ and $PbMoO_4$. There is no such essential mass effect in Ba, Sr and Ca –sheelites. A monotonous growth of internal vibration frequencies is observed in Ba, Sr and Ca–sheelites melts that correlates with the growth of electronegativity (Fig. 2.5). At the same time the frequency dependence of the highest totally symmetric vibronic mode ν_1 (A_g) have opposite character in the crystalline Ba→Sr→Ca tungstates and molybdates (Fig. 2.3, 2.4). In ref. [2.7] it was called as a "negative mass dependence". This phenomenon cannot be explained by the increase of W-O or Mo-O distance due to lattice expansion as well as due to decreasing the electronegativity of Me^{2+} cation. Two last factors and the growth of Me^{2+} cation mass have to reduce the frequency of ν_1 (A_g) mode in Ca→Sr→Ba sheelites, that contradicts with the frequency growth observed in the experiment. The last frequency growth be explained if the predominant influence on $\nu_1(A_g)$ mode frequency is proposed to be due to Davydov Splitting (DS). In the sheelite lattice the $\nu_1(A_1)$ mode is split into A_g and B_u components due to DS-effect (strong $[WO_4]^{2-}$ or $[MoO_4]^{2-}$ molecular group coupling inside one primitive cell of the crystal (eq.2.1a). If $\nu_1(B_u)$ mode has higher energy, the lowering of the splitting value $\Delta E = \nu_1(B_u) - \nu_1(A_g)$ should result in the growth of the frequency of the lower lying ν_1 (A_g) mode. As mentioned in Ref. [2.7], the value ΔE varies with the change of W−W or Mo–Mo distance in the lattice. The growth of this distance with lattice expansion has to reduce ΔE and to increase ν_1 (A_g) mode frequency in the sheelite series if DS variation exceeds the change due to other effects. However, to obtain ΔE (DS) a problem arises to determine the frequency of $\nu_1(B_u)$ mode, as it is inactive in the Raman and the infrared spectroscopy.

Authors [2.15] estimated the value of ΔE for $CaWO_4$ and $CaMoO_4$ crystals using weak features in the infrared spectra, which were assigned to the forbidden $\nu_1(B_u)$ mode. Following Ref. [2.15] the sign of ΔE was positive for $CaMoO_4$ crystal and negative for $CaWO_4$. From this it follows that tungstates and molybdates should have different $\nu_1(A_g)$ mode dependencies with moving along $Ca \rightarrow Sr \rightarrow Ba$ series, that contradicts with our experimental results (Fig. 2.3, 2.4).

High temperature Raman spectroscopic technique provides another possibility to determine ΔE value. In the melt spontaneous Raman spectrum exhibits the nonsplitted vibrations of $[WO_4]^{2-}$ or $[MoO_4]^{2-}$ tetrahedrons, one can determine the frequency shift of $\nu_1(A_g)$ mode at phase transition from the crystalline state to the melt as, $\Delta = \nu_1(A_g)^{crystal} - \nu_1(A_1)^{melt}$. Assuming a symmetrical behavior of ν_1 mode splitting due to dynamic effect, the value of the splitting (ΔE) should be equal $2 \cdot \Delta$.

The experimental temperature dependencies of $\nu_1(A_g)$ mode frequency from 77 K to the melting point are shown in Figs. 2.8, 2.9. The $\nu_1(A_g)$ mode frequencies are not changed in $BaWO_4$ and $BaMoO_4$ crystals at the melting point while large frequency shifts to higher values are observed in other sheelite crystals during the melting (Fig. 2.1, 2.2, 2.6, 2.8, 2.9). This means that in the crystalline state the energy of $\nu_1(A_g)$ mode is smaller and the $\nu_1(B_u)$ energy should be larger in tungstate and molybdate sheelites. Table 2.2 presents the values ΔE calculated as $\Delta E = 2 \cdot \Delta$, where Δ was measured from Figs.2.1, 2.2, 2.6, 2.8, 2.9. One can see the correlation in the change of ΔE value when moving along the tungstate and molybdate crystal series. The splitting grows with the decrease of the $W-W$ or $Mo-Mo$ distance in the lattice. It equals to zero for large dimension cells in $BaWO_4$ and $BaMoO_4$ crystals and is the largest (52-58 cm^{-1}) in $CaWO_4$ and $CaMoO_4$ with the smallest unit cells and minimal distance between anions (Figs. 2.1, 2.2, 2.6, Table 2.2).

Fig. 2.8. Temperature dependencies of the linewidth (Δv_R) and Raman shift of $v_1(A_g)$ vibration in tungstates in the crystalline and molten states. At the melting points the frequency hops are observed only in $CaWO_4$, $SrWO_4$ and $PbWO_4$ crystals. There is no hop in $BaWO_4$.
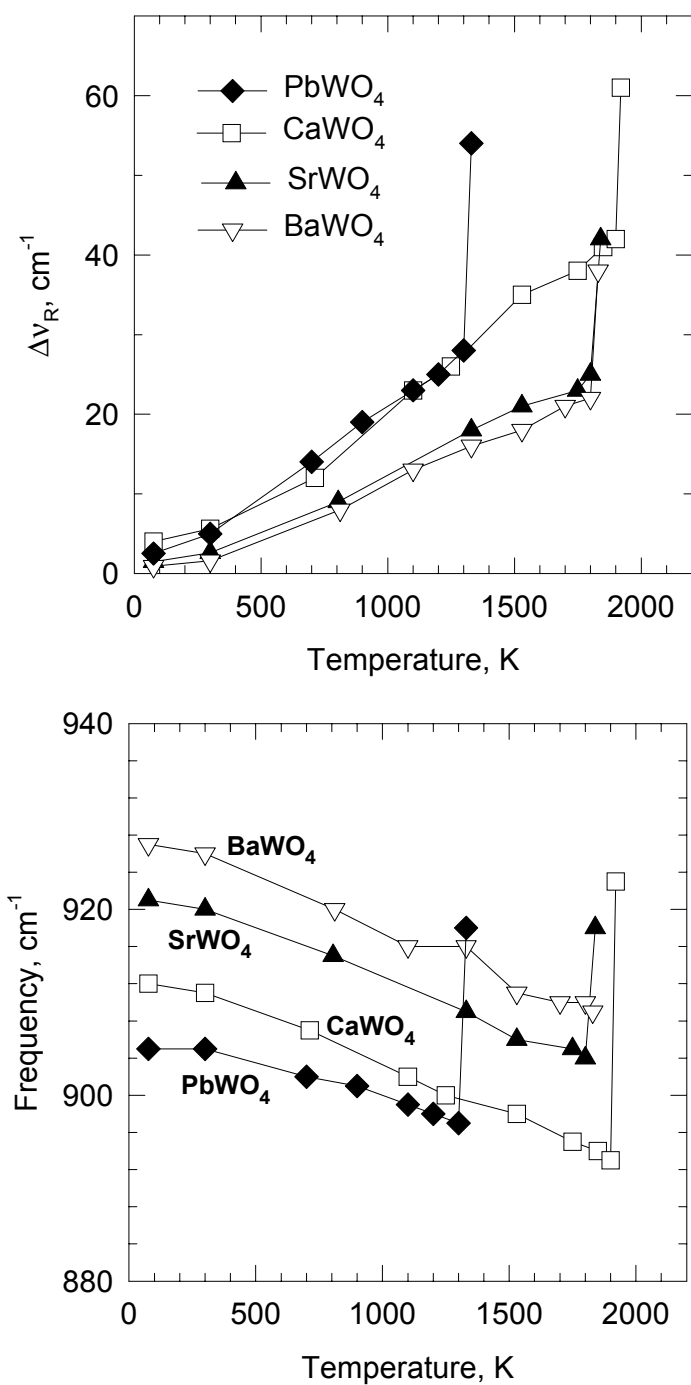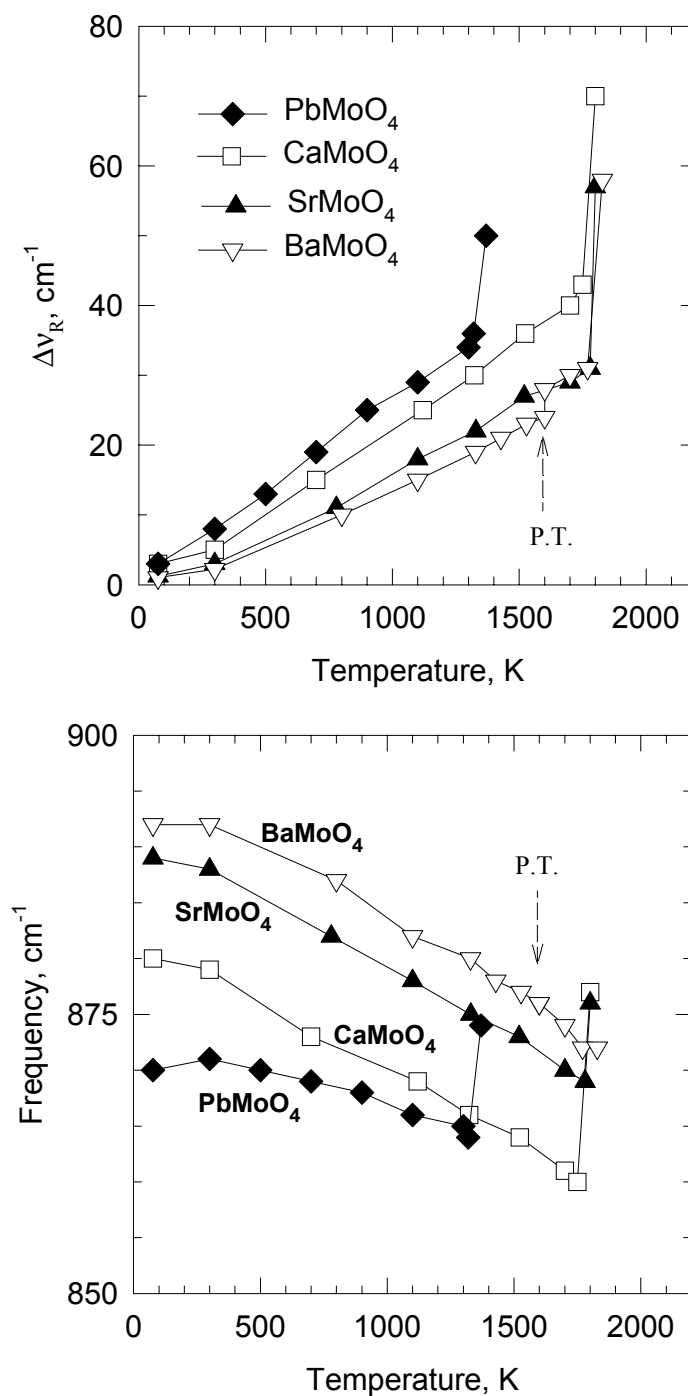
Fig. 9. Temperature dependencies of the linewidth ($\Delta \nu_R$) and Raman shift of $\nu_I(A_g)$ vibration in molybdates in the crystalline and molten states. P.T. – phase transition in $BaMoO_4$ crystal. At the melting points the frequency hops are observed only in $CaMoO_4$, $SrMoO_4$ and $PbMoO_4$ crystals. There is no hop in $BaMoO_4$.

Thus, the reduction of $\nu_1(A_g)$ mode frequencies in Ba→Sr→Ca sheelite series is the result of DS increase. It should be underlined that the growth of DS compensates other factors namely the reduced mass and electronegativity of Me^{2+}-cation, which should increase the frequency of $\nu_1(A_g)$ mode in Ba→Sr→Ca sheelites.

2.3. Results and Discussions

Temperature dependencies of line broadening and frequencies shift for $\nu_1(A_g)$ mode in tungstate and molybdate sheelites show a predominant linear regularity in the temperature region from 300K to the melting point (Figs. 2.8, 2.9). Following Ref. [2.16] at higher temperatures three-phonon relaxation mechanisms of the dephasing and the depopulation for $\nu_1(A_g)$ mode should be proposed. These mechanisms are responsible for homogeneous broadening of the Raman lines. The sheelite lattice vibration scheme (Fig. 2.3) supposes five three-phonon channels for the dephasing and the depopulation of $\nu_1(A_g)$ level:

$$\nu_1(A_g) + \nu_i \rightarrow \nu_1(B_u) \qquad \text{(\textit{dephasing})} \qquad (2.3a)$$

$$\nu_1(A_g) \rightarrow \nu_3(B_g) + \nu_i \qquad \text{(\textit{depopulation})} \qquad (2.3b)$$

$$\nu_1(A_g) \rightarrow \nu_3(E_g) + \nu_i \qquad \text{(\textit{depopulation})} \qquad (2.3c)$$

$$\nu_1(A_g) \rightarrow \nu_3(E_u) + \nu_i \qquad \text{(\textit{depopulation})} \qquad (2.3d)$$

$$\nu_1(A_g) \rightarrow \nu_3(A_u) + \nu_i \qquad \text{(\textit{depopulation})} \qquad (2.3e)$$

The process (2.3a), which involves the $\nu_1(B_u)$ mode, is the phonon up-conversion dephasing process while all other (2.3b-2.3e) result in phonon splitting or decay mechanisms.

The energy gap between the $\nu_1(A_g)$ mode and nearby lower energy vibrons $\nu_3(B_g)$ and $\nu_3(E_g)$ is about 70-150 cm^{-1} for tungstates and 30-130 cm^{-1} for molybdates (Fig. 2.3). For these energy gap values one can find appropriate phonons among $\nu_{f.r.}$ and $\nu_{ext.}$ modes or even acoustic modes to describe the three-phonon relaxation process. It is very complicated to predict the exact

relaxation channel because only phonons with **K**=0 wavevector (the center of Brillouin zone) are active in the Raman and infrared spectra and their dispersion curves are not known. Nevertheless, it is possible to draw some qualitative conclusions on the relaxation (dephasing) mechanism in the sheelites using Raman spectroscopy.

The energy level scheme of internal vibrons for $[WO_4]^{2-}$ or $[MoO_4]^{2-}$ tetrahedron anions differs essentially from that for triangle $[NO_3]^-$ anions in $Ba(NO_3)_2$ and $NaNO_3$ crystals. In $Ba(NO_3)_2$ the energy gap between the internal $\nu_1(A_g)$ mode frequency and the nearby modes is about 300 cm^{-1}. This is the reason of forbidden three-phonon splitting and dephasing processes. In this case four-phonon relaxation processes play dominant role resulting in low probability and extremely small homogeneous broadening of $\nu_1(A_g)$ Raman active mode [2.3]. Consequently, high Raman scattering peak cross section and SRS gain coefficient at moderate integral cross section were registered in this crystal.

High integral Raman scattering cross section for $[WO_4]^{2-}$ and $[MoO_4]^{2-}$ tetrahedron units 2.5 times higher than that in $Ba(NO_3)_2$ allows to obtain efficient SRS in some tungstate and molybdate crystals. From Table 2.2 follows that all tungstates and molybdates exhibit close values of integral Raman scattering cross section. $BaWO_4$ and $BaMoO_4$ crystals show the narrowest homogeneous linewidth ($\Delta\nu_R$ =1.6 and 2.2 cm^{-1} at 300 K) of $\nu_1(A_g)$ Raman mode while other sheelite crystals exhibit broader linewidths up to 6 cm^{-1}. It should be noted that the linewidth is narrowed while moving along Ca→Sr→Ba tungstates and molybdates series. Thus $BaWO_4$ and $BaMoO_4$ crystals have high peak Raman scattering cross sections and are very promising and efficient SRS.

The breakdown of the energy conservation law in the splitting or decay relaxation channels (3b-3e) can cause such regularity. The energy gap between $\nu_1(A_g)$ and $\nu_3(B_g)$, $\nu_3(E_g)$ levels is increased while both $\nu_{f.r.}$ and $\nu_{ext.}$ mode frequencies are significantly reduced with increasing the Me^{2+} cation mass and lattice constants in Ca→Sr→Ba series (Figs. 2.3, 2.4, Table 2.2). At

the same time the $\nu_{ext.}$ mode energy is considerably decreased in PbWO$_4$ and PbMoO$_4$ due to large mass of Pb^{2+} cation. However, such decrease is not accompanied by lowering the $\nu_{f.r.}$ mode frequencies and the growth of the energy gap between $\nu_1(A_g)$ and $\nu_3(B_g)$, $\nu_3(E_g)$ levels which was registered for Ca→Sr→Ba -sheelites (Fig. 2.3). Thus, energy scheme for vibrational levels of PbWO$_4$ and PbMoO$_4$ does not create such difficulties for splitting or decay relaxation mechanisms, which can take place for the BaWO$_4$ and BaMoO$_4$. It can be one of the reasons of the larger linewidth (5 cm^{-1}) of $\nu_1(A_g)$ mode in Pb sheelites in comparison with Ba-crystal (1.6 - 2 cm^{-1}).

Let us consider the up-conversion dephasing process and their influence on Raman mode linewidth of $\Delta\nu_R$ in tungstate and molybdate series. There is only one three-phonon up-conversion process $\nu_1(A_g) + \nu_i \rightarrow \nu_1(B_u)$ which allows the absorption of lattice acoustic or optical phonons of ν_i -energy. The energy splitting $\nu_1(B_u) - \nu_1(A_g) = \Delta E$ is negligible for BaWO$_4$ and BaMoO$_4$ (Table 2.2). This means that the probability of up-conversion processes in these sheelites is low due to small density of states ($\rho \sim \nu_i^2$) of acoustic phonon (as well as optical) with $\nu_i \approx 0$. Consequently, the narrowest linewidth $\Delta\nu_R$ was registered in BaWO$_4$ and BaMoO$_4$ crystals. An increase of ΔE_1 value correlates with the growth of $\Delta\nu_R$ in Ba→Sr→Ca series of tungstates and molybdates (Table 2.2). Thus, the up-conversion dephasing channel appears to be important in the relaxation mechanism of broadening of $\nu_1(A_g)$ Raman mode in sheelite crystals and can be diminished only by cooling the crystal down to $kT < \Delta E_1$.

Spontaneous Raman spectroscopic experiments revealed the dependencies of vibrational spectra of sheelite crystals on the mass, size and basicity of Me^{2+} cation. The effect of cation mass was found to be predominant for low energy, external vibrations. The internal vibrational mode frequencies exhibited dependence on lattice parameters and the degree of the partially covalent bond between the cation and molecular ionic group [WO$_4$] and [MoO$_4$]. It was found

that Davydov splitting of totally symmetric ν_1 valence vibration of [WO$_4$] and [MoO$_4$] tetrahedrons grows in the series Ba→Sr→Ca sheelites.

The above experiments have shown the essential dependence of the bandwidth of $\nu_1(A_g)$ − Raman mode on the peculiarities of crystal lattice and the sort of Me^{2+} cation in series of MeWO$_4$ and MeMoO$_4$ (Me = Ca, Sr, Ba, Pb) crystals with sheelite structure. The combination of a heavy Me − cation and large interionic distance in the lattice results in low probability of up-conversion and phonon splitting relaxation processes in BaWO$_4$ and BaMoO$_4$ crystals. The narrowest linewidth of $\nu_1(A_g)$ Raman mode (1.6 cm^{-1} and 2.2 cm^{-1}) provides high value of SRS gain coefficient in these crystals at room temperature. These media can be proposed as effective nonlinear materials for developing Raman shifters. This was proved in the laser experiments recently [2.17].

Our experiments showed also that the reduction of the frequencies of ν_{ext} vibration spectrum is not the only factor that lowers the probability of all relaxation mechanisms in sheelite structure. Opposite to BaWO$_4$ and BaMoO$_4$ crystals, the largest mass of Pb^{2+} -cation did not result in the phenomenon of narrowing $\nu_1(A_g)$ Raman line in PbWO$_4$ and PbMoO$_4$.

References to chapter 2

1. T. T. Basiev, A. A. Sobol, P. G. Zverev, V. V. Osiko, and R. C. Powell, Applied Optics, **38** (1999) 594-598.

2. T. T. Basiev, A. A. Sobol, P. G. Zverev, L. I. Ivleva, V. V. Osiko and R. C. Powell, Optical materials **11** (1999) 307-314.

3. P. G. Zverev, T. T. Basiev, V. V. Osiko, A. M. Kulkov, V. N. Voitsekovskii and V. E Yakobson, Optical Materials **11** (1998) 315-334.

4. Yu. K. Voronko, A. B. Kudrayvtsev, V. V. Osiko and A. A. Sobol, Growth of Crystals **16** (1988) 199-217, (ed. by Kh. S. Bagdasarov Consultant Bureau.N.Y.).

5. S. P. S. Porto and J. E. Scott, Phys. Rev. **157** (1967) 716-719.

6. J. F. Scott , J. Chem. Phys. **48** (1968) 874-876.

7. J. F. Scott , J. Chem. Phys. **49** (1968) 98-100.

8. R. K. Khanna, W. S. Brower, B. R. Guscott and E. R. Lippinatt, J. Res. Nat. Boreou of Stand.**72A** (1968) 81-84.

9. H. Kanamori, S. Hayashi and Y. Ikeda, J. Phys. Soc. Japan **36** (1964) 511-516.

10. H.Poulet and J.P.Mathieu, «Spectres de vibration et symmetric des cristaux», Publisher «Gordon and Breach», Paris,(1970).

11. R. T. Sanderson, Chemical bonds and bond energy, Academic Press, 1976.

12. Phase diagrams of the system of hard melting oxides, issue II, part 4, ed. by F. D. Balashov, Leningrad, Nauka (1988).

13. A. N. Lasarev, A. P. Mirgorodskii and I. S. Ignatiev, «Vibration spectra of complicated oxides», Publisher «Nauka» Leningrad (1975).

14. O. S Philipenko, E. A. Pobedimskaia and N.N.Belov, Krystallographia **13,** (1968) 163-165

15. A. S. Barker and Jr. , Phys. Rev. **135** (1964) 742.

16. A. A. Maradudin and R. G. Wallis, Phys. Rev. **123** (1961) 777-789.

17. P. G. Zverev, T. T. Basiev, A. A. Sobol, V. V. Skornyakov, L. I. Ivleva, N. M. Polozkov and V. V. Osiko, Quantum Electronics **30**,(2000) 55-59.

3. The growth technique of alkali earth tungstate and molybdate crystals for Raman lasers.

The experiments on the single crystal growth of $BaWO_4$, $CaMoO_4$, $SrMoO_4$ samples by Czochralski technique from the melt in the air were done in frames of the work on this project. The special attention was made for producing oriented crystals with high optical quality for future laser applications.

An industrial crystal growth installation "Crystal-2M" was used for radio frequency heating of platinum crucible and pooling the crystal (Fig. 3.1). The starting materials were prepared from highly pure components: $BaCO_3$, $CaCO_3$, $SrCO_3$, MoO_3, WO_3. The components were weighed with an accuracy of 0.1 mg in accordance with the desired stoichiometry. Their mixture was prepared in the mechanical mill. The mixture of starting materials was heated to $1000 \div 1200$ C and fired during $5 \div 6$ hours in a resistance furnace KO-14 type. The reaction product was analyzed by X-ray method to confirm the completion of the chemical reaction that is the absence of any X-ray patterns of the constituent components. The polycrystalline powders were used as charges. The melt was contained within 100 cm^3 platinum crucible which was embedded in thermal insulation. Melt homogenization lasted for $1 \div 2$ hours at $1500 \div 1580$ C. The pulling rate ranged from 4 to 10 mm/h, rotation speed was from 20 to 35 rpm. The vertical thermal gradient varied from 60 to $100^oC/cm$.

The seed crystal was oriented along (100), (110), or (001) direction. For growth conditions optimization and formation of flat crystallization front, the position of the afterheater above the crucible can be varied and the rotation rate can be increased up to 100 rpm for higher thermal gradients. For molybdates it was found that the volume crystallization rate should be decreased from 9 cm^3/h for nominally pure crystals down to 7 cm^3/h for doped crystals. The cooling time of grown crystals was $15 \div 30$ h.

The grown crystals were transparent in the visible spectral range (in absence of activator ions), and were crack-free. They had minimal number of scattering centers, which were observed under laser irradiation.

It is known that when $CaMoO_4$ is grown by itself it tends to lose oxygen and turns blue due to Mo^{6+} to Mo^{4+} valence transition. Such a colored crystal can be reoxidized under additional annealing at about 1300 C, but this is rather undesirable procedure. The coloration of the crystal results in the parasitic absorption and lower laser damage threshold. In one of the experiments for nominally pure $CaMoO_4$ the laser damage threshold was measured to be 80 MW/cm^2 for single pulse regime with 12 ns pulse duration and 14 mJ pulse energy. It was possible to reduce the coloration of the crystal by adding the small amount of chromium niobate into the $CaMoO_4$ melt. In such a way it was stabilized to the point where no oxygen loss and hence no coloration occurs. The laser damage threshold for Cr doped $CaMoO_4$ crystal was increased up to 1200 MW/cm^2. No any coloration was observed in $BaWO_4$ crystal.

The cross-section of the crystals grown along c-axis was almost round while for crystals grown along a-axis it was elliptical. In the case of $BaWO_4$ the excess of WO_3 (0.5-1.5 wt. %) was also added to the melt of stoichiometric composition to eliminate the presence of scattering centers in the growing crystals. The high optical quality $BaWO_4$ crystals were grown from the melt composition with l wt. % WO_3 excess.

Our spectroscopic data has shown that the highest Raman gain in $BaWO_4$ crystal was observed when the excitation electric vector was parallel to the crystallographic axis. So to get high Raman gain the pooling axis of the seed crystal was oriented perpendicular to C_4 axis. The cross section of the crystals grown along this direction had elliptical shape. The boules were up to 60 mm long and 20 mm in diameter (Fig. 3.2). This allowed to prepare optical elements with dimensions 8x8x31 mm, 5x5x45 mm of high optical quality and to test them in the experiments on the stimulated Raman scattering (Fig. 3.3).

Fig. 3.1. The crystal growth installation CRYSTALL-3M which was used for growing CaMoO$_4$, SrMoO$_4$ and BaWO$_4$ crystals.
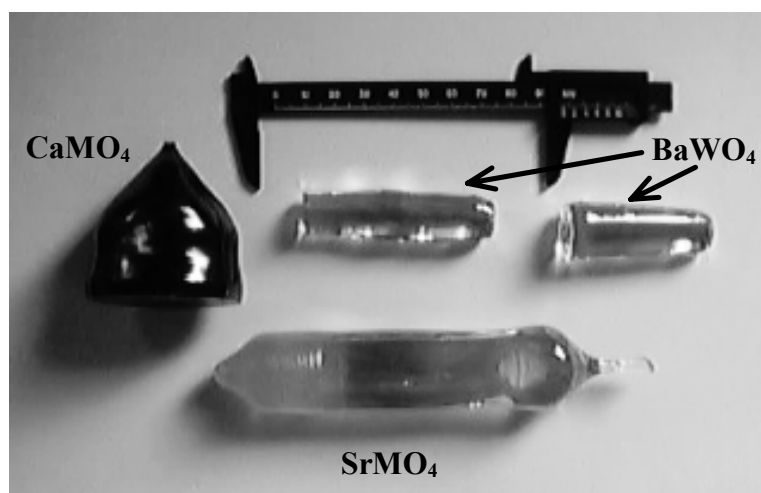
Fig. 3.2. The boules of $CaMoO_4$, $SrMoO_4$ and $BaWO_4$ crystals.
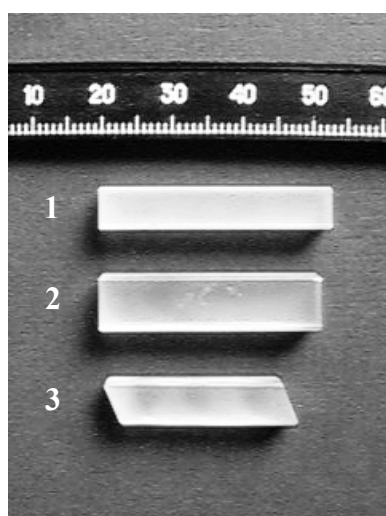

Fig. 3.3. The experimental samples of $BaWO_4$ crystals

1,2 -plane-parallel, 3 - Brewster.

4. Stimulated Raman scattering measurements in the new high efficient BaWO$_4$ Raman crystal

4.1. SRS energy and threshold measurements

As mentioned above the results on spontaneous Raman spectroscopy allows to predict the perspectives of a medium for Raman laser development. SRS threshold measurements provide with the real value of the Raman gain coefficient of the certain Raman material. Below we will describe our SRS threshold experiment.

The optical scheme of the experimental setup for SRS threshold measurements is presented in Fig. 4.1. Pulsed-periodic single mode Nd^{3+}:YAG laser with passive Q-switching in LiF:F$_2^-$ color center crystal was used as a pump source. Pump pulse duration was 10 ns with 10 pulses per second repetition rate and the pulse energy was about 40 mJ at 1.064 μm wavelength. The KTP second harmonic doubler (5x5x7 mm^3) could be used to proceed SRS threshold measurements in the visible spectral range at 532 nm wavelength.

The pump energy at the entrance of the nonlinear Raman crystal was smoothly controlled by an appropriate retardation plate and Glan polarizer. To control the pump laser energy, part of it was reflected by a glass plate to the photodiode. The scattered Stokes radiation was collimated by the lens and spectrally selected by the diffraction grating. The scattered energy was measured with the photodiode. The scattered and pump beams were measured simultaneously by the digital oscilloscope Tektronix TDS-380. Due to the fluctuation of the pump energy the intensity of the scattered Stokes beam changed from pulse to pulse. The digital registration system allowed us to make the single pulse measurements that increased the accuracy of SRS threshold measurements.
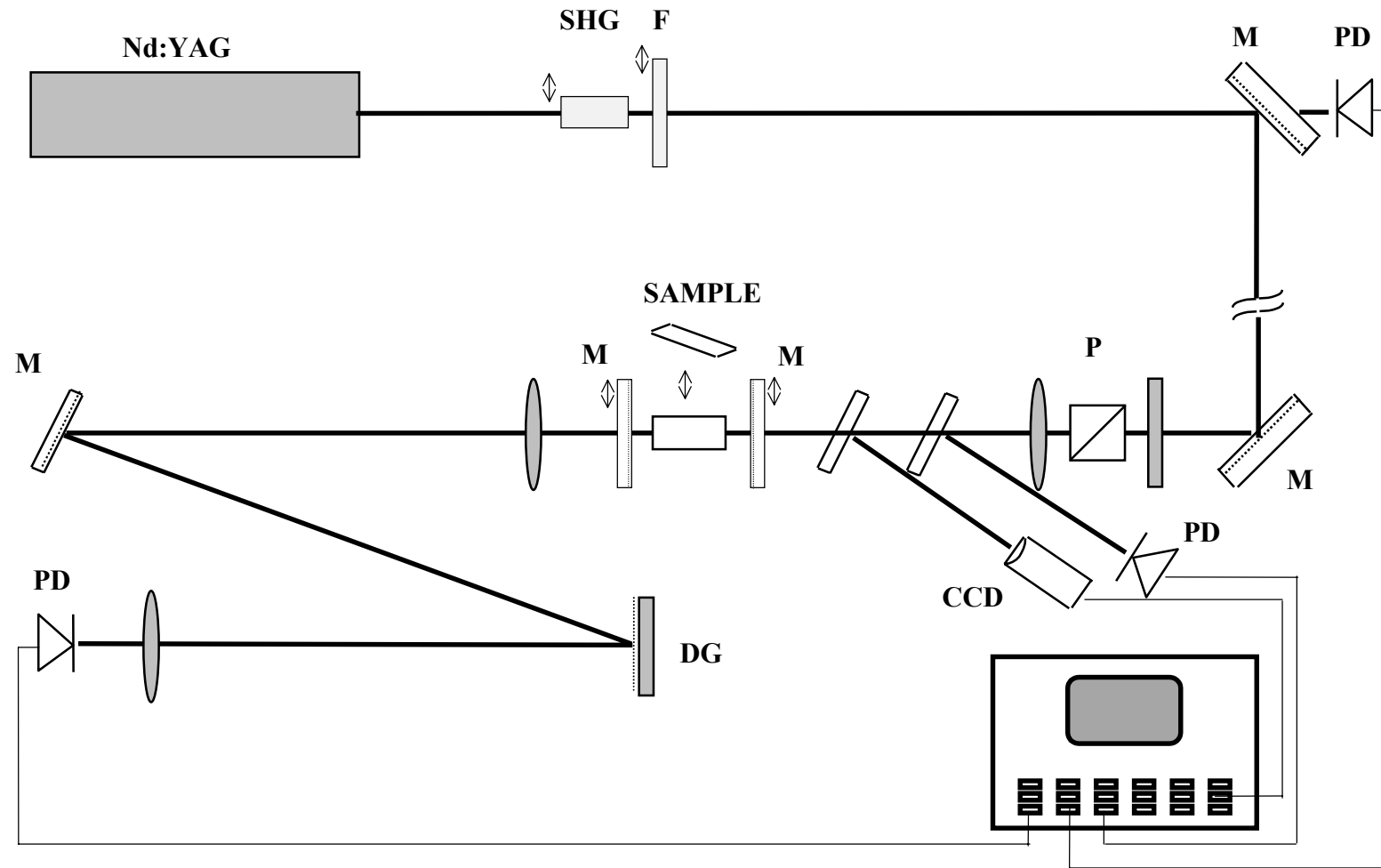
Fig. 4.1. Experimental setup for SRS threshold measurements.

Nd^{3+}:YAG laser with passive Q-switching working in TEM$_{00}$ mode, SHG - KTP second harmonic generator, F - color glass filter, $\lambda/2$ - half wavelength retardation plate, P - Glan polariser, SAMPLE - nonlinear Raman crystal, DG -diffraction grating, PD - photo diodes, CCD - CCD camera, M - mirrors.

The pulse duration was about 12 ns at 1064 nm wavelength and 10 ns at 532 nm. It was controlled by Ge avalanche photodiode and Tektronix TDS-380 digital oscilloscope with total temporal resolution of 0.5 ns. The pump pulse duration was measured in each set of the experiments.

The pump radiation was focused into the investigated sample by lenses with 50 cm and 80 cm focal lengths. The spatial profile of the pump in the focal region was continuously controlled by reflecting part of the beam to CCD camera connected with PC. The spatial profile had good Gaussian shape. The beam diameter at half maximum was measured to be about 90 μm for lens with $f_1 = 50$ cm focal length and about 170 μm for $f_2 = 80$ cm for 1064 nm wavelength.

The conditions of the pump focusing into the investigated sample essentially effect on the measured SRS threshold value. There are two parameters which characterize the focal point, the focal spot size ($2w_0$) and the waist length or the Depth of Focus (*DOF*). Let's calculate the parameters of the laser beam focus used in our experiment. The transverse distribution of the pump beam radiation had a smooth Gaussian shape, so we could use Gaussian formalism to estimate the required parameters.

The Gaussian intensity distribution is a radially symmetrical distribution whose electric field intensity in transversal direction is given by

$$E_S = E_O \exp\left\{ -r^2 \Big/ w_O^2 \right\} \tag{4.1}$$

This kind of distribution is usually observed at the output of the laser that works in TEM_{00} mode. The parameter w_0 is usually called the Gaussian beam radius and denotes the radius at which the intensity has decreased to $1/e^2$ times of its value at the axis. The far-field for the Gaussian beam is the distance x from the laser which satisfies equation $\lambda x > \pi w_0^2$. For our experimental setup with 1 mm intracavity laser aperture ($w_0 = 1$ mm) at 1064 nm wavelength the far-field can be considered at the distance of $x > 3$ *m*. This satisfies our experimental conditions

where the distance from the laser to Glan prism was more than 4 meters (Fig. 4.1). The focusing of the Gaussian beam with diameter D by the lens with focal length f provides the beam waist with the spot size $2w_0$:

$$2w_0 = \left(\frac{4\lambda}{\pi}\right)\left(\frac{f}{D}\right) \qquad (4.2)$$

The depth of focus (waist length) DOF is usually defined as the distance between the values of x where the beam is $\sqrt{2}$ times larger than it is at the beam waist. It equals as following:

$$DOF = \left(\frac{8\lambda}{\pi}\right)\left(\frac{f}{D}\right)^2 \qquad (4.3)$$

We used two lenses ($f_1 = 50$ cm and $f_2 = 80$ cm) for focusing the pump radiation into the samples in our experiments. The beam size at the lens was about 4 mm for 1064 nm wavelength and 3 mm for 532 nm. Table 4.1 shows the calculated parameters of the focus in these cases.

From Table 4.1 follows that for the lens $f_1 = 50$ cm the waist of the beam is 1.5 times smaller and thus it is easier to reach the SRS threshold intensity. At the same time there will be a shorter waist and longer crystals will give larger mistake due to the change of the beam diameter and pump intensity. The experimental waist size well correlates to the calculated values.

Table 4.1. The calculated and measured focus spot sizes and calculated waist length of the focused Gaussian beam in experiments.

λ [nm]	f [cm]	$2w_0$ [μm]		DOF [cm]
		calculated for 1/2 level	measured at 1/2 level	
1064	50	90	90	4.0
1064	80	170	170	10
532	50	75	-	3.5
532	80	120	120	9.0

The SRS threshold measurements were done at $\lambda = 1064$ nm and $\lambda = 532$ nm wavelengths for plane-parallel crystals $BaWO_4$ (31 mm), $KGd(WO_4)_2$ (36 mm) and $Ba(NO_3)_2$ (50 mm and 25 mm). The experimental curves of the SRS scattering versus pump energy are shown in Fig. 4.2 - 4.4. The experimental results are summarized in Table 4.2. To work at pump intensities lower than the laser damage threshold all samples were placed into additional Raman cavity 18 cm long which was composed by two flat dichroic mirrors, entrance mirror ($R_{1.064} <$ 5%, $R_{1.1-1.25} > 98\%$) and output coupler ($R_{1-1.2} \sim 55\%$). As it was shown earlier the use of the additional cavity allows us to reduce the SRS threshold [4.1].

When the pump radiation (1064 nm) was focused by the lens $f_1 = 50$ cm, the SRS threshold in barium nitrate crystals with two lengths (50 mm and 25 mm) was observed at 0.5 mJ and 0.65 mJ pump energies, correspondingly and practically doesn't depend on the length of the crystal due to small DOF=40 mm. The use of the lens with longer focal length $f_2 = 80$ cm, longer DOF=10cm and larger waist diameter $2w_0$ resulted in the increase of the SRS threshold energies to 1.0 mJ for 50 mm crystal and 1.6 mJ for 25 mm one. So for short crystal (25 mm) the SRS threshold energy with lens f_1 was approximately 3 times higher than that for longer lens f_2 due to 3 times higher pump intensity in the focal point. At the same time the smaller beam waist $2w_0$ resulted in the shorter waist length (DOF). This considerably changed the density of the pump energy in the long crystal (50 mm). The SRS threshold energy was achieved only in the short central part of the crystal. As a result the small difference in the threshold values was observed for f_1 lens for two crystals with different lengths.

From Table 4.1 follows that the use of the longer lens $f_2 = 80$ cm provides the DOF of about 10 cm which becomes longer than the crystal length. In this case the threshold energy must linearly depend on the crystal lengths. Meanwhile our experimental results show that the uniform distribution along the crystal can be considered only for the shorter crystal (25 mm) and one can properly calculate SRS threshold only in this case.
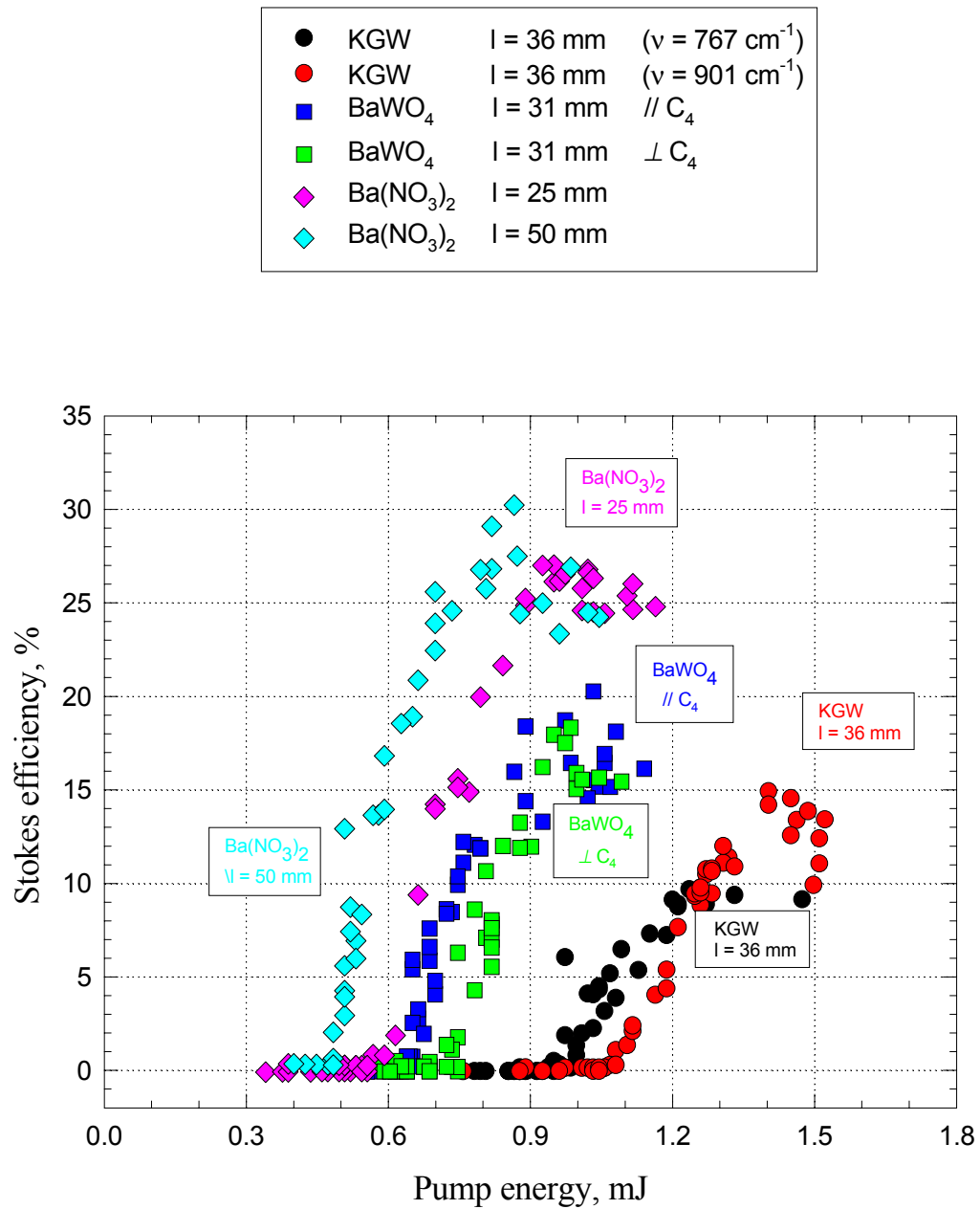
Fig. 4.2. The pump dependence of the Stokes efficiency under irradiation with 1064 nm wavelength and focusing with lens $f_1=50$ cm ($2w_0=90$ μm) in KGd(WO$_4$)$_2$ (36 mm), Ba(NO$_3$)$_2$ (25 and 50 mm), BaWO$_4$ (31 mm, two polarizations). The crystals were placed into the cavity.
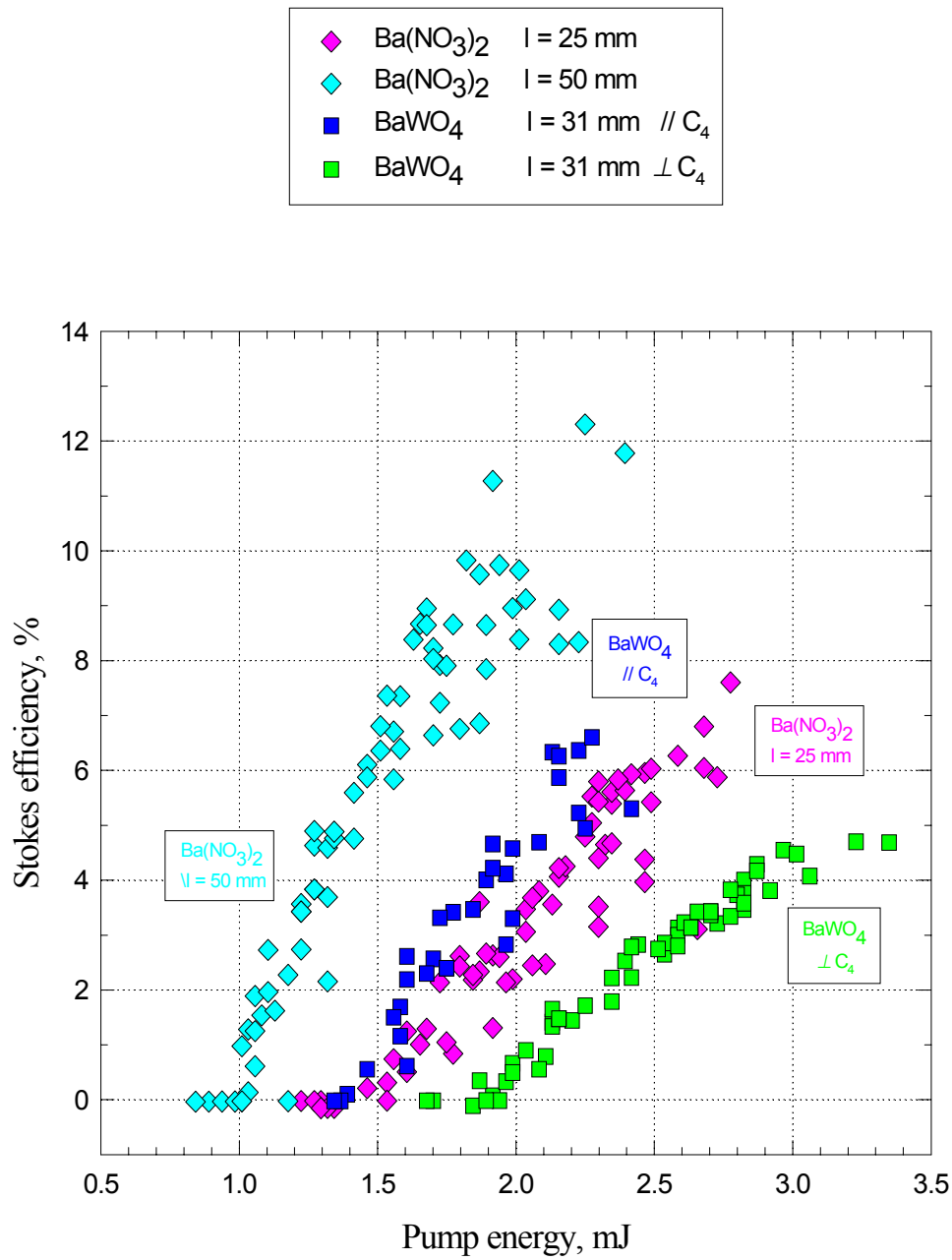
Fig. 4.3. The pump dependence of the Stokes efficiency under irradiation with 1064 nm wavelength and focusing with lens $f_2=80\ cm$ ($2w_0=170\ \mu m$) in Ba(NO$_3$)$_2$ (25 and 50 mm), BaWO$_4$ (31 mm, both polarizations). The crystals were placed into the cavity.
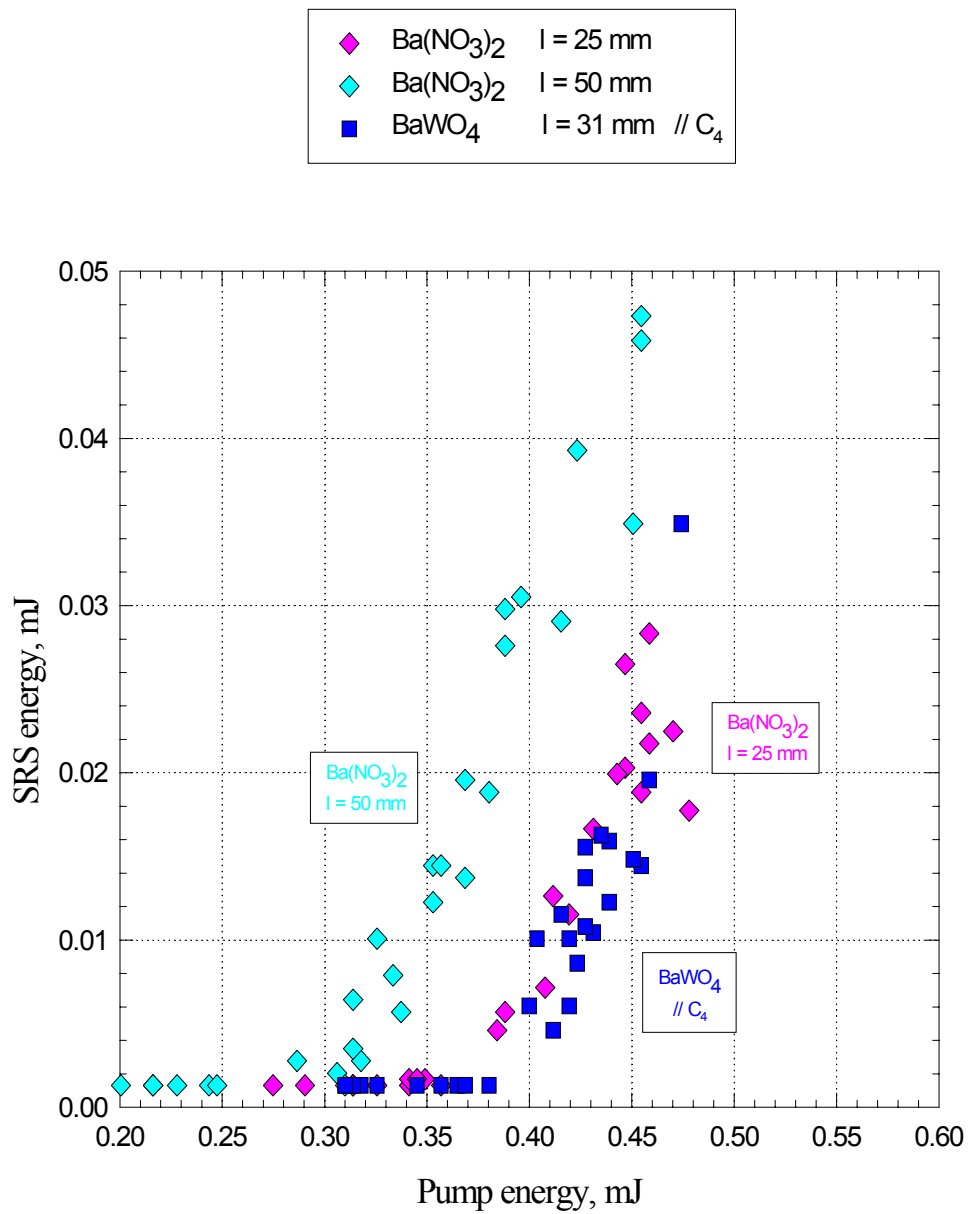
Fig. 4.4. The pump dependence of SRS scattering energy under irradiation with 532 nm wavelength and focusing with lens $f_2=80\ cm$ ($2w_0=120\ \mu m$) in $Ba(NO_3)_2$ (25 and 50 mm), $BaWO_4$ (31 mm) plane-parallel crystals without external cavity.

The lengths of $BaWO_4$ (31 mm long) and $Ba(NO_3)_2$ (25 mm) were close to each other so we considered that for calculation of the SRS threshold gain the uniform distribution of the pump could be considered for both crystals. The SRS threshold energies measured in these crystals were close to each other that proves that $BaWO_4$ and $Ba(NO_3)_2$ crystals have close values of the Raman gain coefficient.

The SRS gain coefficient is much higher for the visible radiation. The Raman gain coefficient in $Ba(NO_3)_2$ was measured to be 11 cm/GW [4.2] for 1064 nm pumping and 47 cm/GW for 532 nm wavelength [4.3]. This fact allowed us to make measurements under pumping with 532 nm wavelength without any additional Raman cavity and without laser damage. Fig. 4.4 and the right column in Table 4.2 present SRS threshold energies in this case.

Another phenomena which can influence the value in the SRS threshold measurements is the reflection of the scattered radiation from crystal faces. Previously in was mentioned that by placing the Raman crystal into the cavity it was possible to reduce the SRS threshold energy [4.1]. In our experiments it was noted that when the sample is aligned perpendicular to the pump beam axis then the threshold value is significantly reduced. This effect is due to the reflection of the Stokes radiation from the crystal faces and its consequent amplification on the way back and

Table 4.2. The measured SRS threshold energies [mJ] in $Ba(NO_3)_2$ and $BaWO_4$ crystals under various focusing conditions.

Material	length	Threshold Energy [mJ]		
	[mm]	$\lambda = 1064$ nm		$\lambda = 532$ nm
		$f_1 = 50$ cm	$f_2 = 80$ cm	$f_2 = 80$ cm
$Ba(NO_3)_2$	50	0.5	1.0	0.31
$Ba(NO_3)_2$	25	0.65	1.6	0.38
$BaWO_4$	31	0.65	1.5	0.40

forward inside the crystal. This effect is so strong that for plane-parallel crystal even in case of its some misalignment, the scattered radiation propagates not along the pump beam where the gain is highest but perpendicular to the crystal faces which work like a cavity for SRS. The refraction coefficient of $Ba(NO_3)_2$ crystal is 1.56 and for $BaWO_4$ is ~1.85, this corresponds to the Fresnel reflection at each crystal face of 4% and 6%, correspondingly. Due to the exponential behavior of the SRS amplification this small reflection can considerably influence the SRS threshold value.

To diminish this resonator effect we used samples with Brewster faces. $Ba(NO_3)_2$ (40 mm long) and $BaWO_4$ (25 mm long) crystals with Brewster cut faces were prepared for these experiments. The experimental results for the lens $f_2 = 80$ cm with pump dependencies of the SRS energy at 532 nm wavelength without Raman cavity are shown in Fig. 4.5 and summarized in Table 4.3. For $Ba(NO_3)_2$ crystal the SRS threshold energy was measured to be 0.65 mJ for Brewster element and 0.3 mJ for plane-parallel. And for $BaWO_4$ crystal the threshold was 1.20 mJ and 0.25 mJ correspondingly. Thus, one can see that when the crystal faces are oriented perpendicularly to pump radiation axis, the SRS threshold energy is dramatically reduced and for $BaWO_4$ crystal even less then for $Ba(NO_3)_2$.

The specially developed computer program allowed us to calculate the Raman gain coefficient from the real experimental data. It uses real temporal and spatial pump distributions in the sample, and in the plane wave approximation calculates the SRS threshold energy. The experiments on Brewster crystals provided us with the values for single pass SRS amplification and it was possible to find that the Raman gain coefficient equals to 36 cm/GW in $BaWO_4$ crystal and 52 cm/GW in $Ba(NO_3)_2$ crystal with the accuracy of 10%.

From Fig. 4.2 one can see that the real SRS conversion efficiency in $BaWO_4$ crystal under 1064 nm pumping in the external cavity was measured to be up to 20% which corresponds to 22% quantum conversion efficiency.

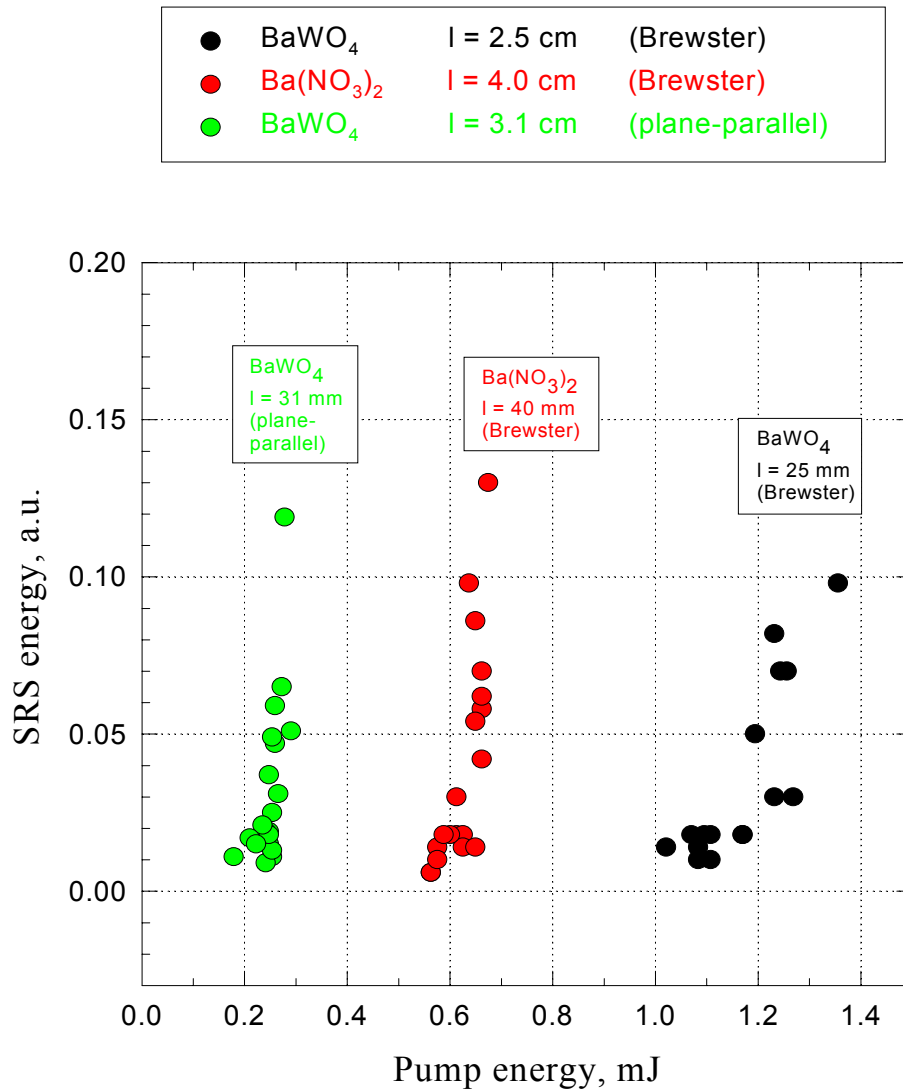Fig. 4.5. The pump dependence of SRS scattering energy under irradiation with 532 nm wavelength and focusing with lens $f_2=80 \ cm$ ($2w_0=120 \ \mu m$) in Brewster Ba(NO$_3$)$_2$ (40 mm), Brewster BaWO$_4$ (25 mm) and plane parallel BaWO$_4$ (31 mm) without external cavity.

Table 4.3. The measured SRS threshold energies [mJ] in plane-parallel and Brewster $Ba(NO_3)_2$ and $BaWO_4$ samples at 532 nm wavelength with lens f_2 = 80 cm.

Material		length [mm]	E^{thresh} [mJ]	G_{532} [cm/GW]
$Ba(NO_3)_2$	plane-parallel	25	0.3[*]	
$Ba(NO_3)_2$	Brewster	40	0.65	52
$BaWO_4$	plane-parallel	31	0.25	
$BaWO_4$	Brewster	25	1.20	36

* - another set of experiments

No saturation was observed in the behavior of this dependence and the further increase of the pump energy can result in the consequent increase of the conversion efficiency. The differential or slope efficiency showed for $BaWO_4$ crystal high value η_{slope} = 75%, close to that observed for $Ba(NO_3)_2$ crystal and much higher than that for $KGd(WO_4)_2$ crystal (η_{slope} = 30%).

Our measurements of the SRS threshold showed that for longer wavelength the SRS gain coefficient is strongly reduced. In Table 4.4 we summarize the results of SRS gain measurements in $BaWO_4$ crystal with different wavelength pumping and predict the gain at 1.3 μm wavelength.

Table 4.4. The Raman gain coefficient in $BaWO_4$ crystal at different pumping wavelengths.

Pump wavelength, nm	Raman gain coefficient, cm/GW
532	35
1064	8.5
1300	5.8

One can see that for near IR pump radiation the Raman gain becomes considerably lower than that for visible. That's why for near IR special precautions must be made to reduce the SRS threshold in order to obtain high conversion efficiency at pump intensities lower than the optical damage power. As we have seen above this can include placing of the Raman crystal into the special Raman cavity and aligning its surfaces perpendicular to the beam axis. The SRS threshold can be reached by increasing the pump intensity due to shorter pump pulses. This can be done by use of the picosecond pump pulses or of the nanosecond pulses with subnanosecond temporal structure.

4.2. SRS of picosecond pulses in BaWO$_4$ Raman laser

Due to great improvements in the development of short pulse laser systems with high peak power, we were interested to investigate SRS of picosecond pulses. Use of subnanosecond and picosecond pump pulses provide easy way to exceed SRS threshold and to increase laser damage threshold of Raman crystal. The main problem arises due to the transient behavior of SRS when pump pulse duration becomes comparable or shorter than the vibron relaxation time T_2 in Raman crystal which is inversely proportional to Raman line broadening $T_2 \sim (\Delta v)^{-1}$.

Well known Ba(NO$_3$)$_2$ Raman crystal shows unfavourable properties for scattering the pump radiation with picosecond pulse duration of 25 ps, as its gain decreases about ten times compared with nanosecond pump regime [4.4]. This is a consequence of the transient behaviour of SRS in barium nitrate due to long relaxation time of the excited Raman vibrations ($T_2 = 26$ ps). KGd(WO$_4$)$_2$ crystal has about 2 times lower value of steady state Raman gain, comparing to Ba(NO$_3$)$_2$, but shows better SRS properties under picosecond pumping due to broader Raman line and shorter vibrational dephasing time ($T_2 = 5$ ps). Previous measurements showed that KGd(WO$_4$)$_2$ has about three times higher Raman gain than Ba(NO$_3$)$_2$ in similar short 25 ps pulse pumping arrangement [4.5]. From the above follows a requirement of a 'universal' Raman-active

crystal, that would possess high gain in both temporal cases. Below newly developed BaWO$_4$ crystal was investigated for picosecond pumping comparing to Ba(NO$_3$)$_2$ and KGd(WO$_4$)$_2$ crystals.

To investigate the behavior of the new efficient Raman media, the Nd^{3+}:YAG picosecond laser was used. A mode-locked Nd:YAG laser system with a pulse selector generated single pulse radiation at the fundamental wavelength with 40 ps duration. After three amplifiers it provided pulse energy of 100 mJ. The second harmonic output was obtained by doubling in KDP nonlinear crystal and consisted of 28 ps pulses with energy up to 40 mJ. Only part of available output energy was used in our experiments. The laser beam passed through an appropriate polarizer and half wavelength plate, that provided smooth variation of pump energy into the Raman crystal (Fig. 4.6). The diameter of the laser beam was decreased by an aperture and telescope to approximately 1.6 mm at the input face of sample for fundamental and 0.9 mm for second harmonic radiation. Glass plate, serving as a beam splitter, reflected part of the laser radiation into an energy-calibrated Si photodiode connected to a digital oscilloscope (Tektronix TDS 380), which was used to monitor the pump energy. The scattered radiation from the crystal was spectrally selected by a filter and collimated by a lens.

For low energy measurements at the threshold, we used a detection system consisting of
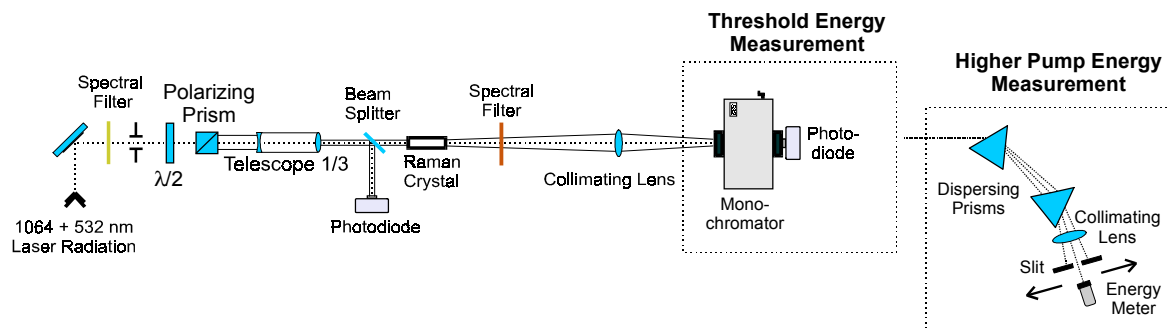

Fig. 4.6. Experimental setup for energy measurement of the pump and the Stokes radiation around SRS threshold conditions and for higher pump energy.

a grating monochromator (Oriel 77250) and two photodiodes (Si for 532 nm pump and Ge for 1064 nm pump) with digital oscilloscope readout. The monochromator was adjusted to transmit radiation of the measured Stokes component and voltage signals from both photodiodes were recorded by oscilloscope simultaneously. At pump energies much above the threshold, when SRS radiation energy sharply increased, we used another experimental arrangement to prevent monochromator grating from being damaged. The collimated scattered radiation was spectrally dispersed by two flint glass prisms and a movable slit. The energy of the certain Stokes component was measured by an energy meter. The losses in the cascade of optical elements were carefully estimated and the values of the measured energy were recalculated. The minimum measurable Stokes energy in this arrangement was about 10 μJ.

The temporal pulse shapes of the first Stokes component and pump radiation were obtained by means of streak camera (VICA 02) with a temporal resolution of 1 ps. The experimental arrangement for temporal streak camera measurements is shown in Fig. 4.7. Incoming optical pulse firstly triggered camera's electronics and then passed an optical delay path of several meters. The triggering signal level, together with time delay, was carefully adjusted to observe the optical pulse image at the camera's fluorescent screen. The observed image was recorded with a CCD camera connected to a PC and its spatial structure reflected the temporal development of the pulse. The processing of the image with commercial graphics
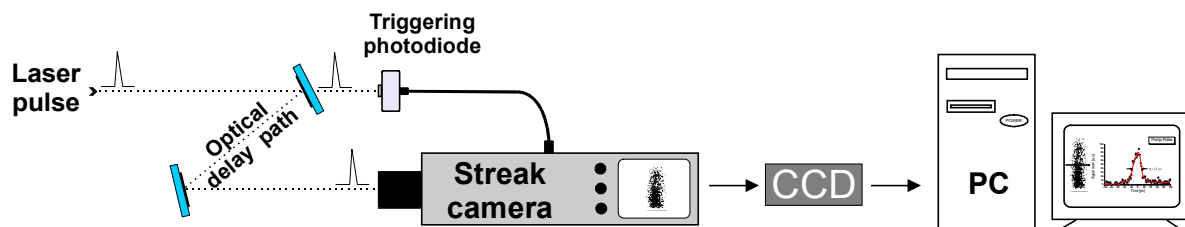

Fig. 4.7. Experimental arrangement for measuring the picosecond temporal profile of laser pulses.

software provided us the temporal pulse structure.

Firstly the detailed energy measurements of the Stokes components were done for 532 nm pump radiation. The energy measurements of the generation thresholds for the first and second Stokes components in crystals used the first type of detection system. The measured values of SRS generation thresholds for first and second Stokes can be found in Table 4.5. As one can see $BaWO_4$ crystal exhibits the threshold energy lower than KGW and KYW crystals which are well known as the leaders for picosecond Raman conversion. At the same time Raman gain for $BaWO_4$ crystal in picosecond regime is at least 3 times higher than that for $Ba(NO_3)_2$. Efficient Stokes conversion was not observed in KYW due to shorter crystal length and poorer optical quality of the available sample. Conversion efficiencies of the Stokes components up to the third order as a function of pump energy for $BaWO_4$ and $KGd(WO_4)_2$ crystals are plotted in Fig 4.8. For the pump energies above 0.5 mJ the second type of the experimental arrangement was used.

Table 4.5. The SRS threshold energies of the first and second Stokes components together with calculated Raman gains for $BaWO_4$, $KGd(WO_4)_2$ and $KY(WO_4)_2$ crystals with 532 nm pump radiation.

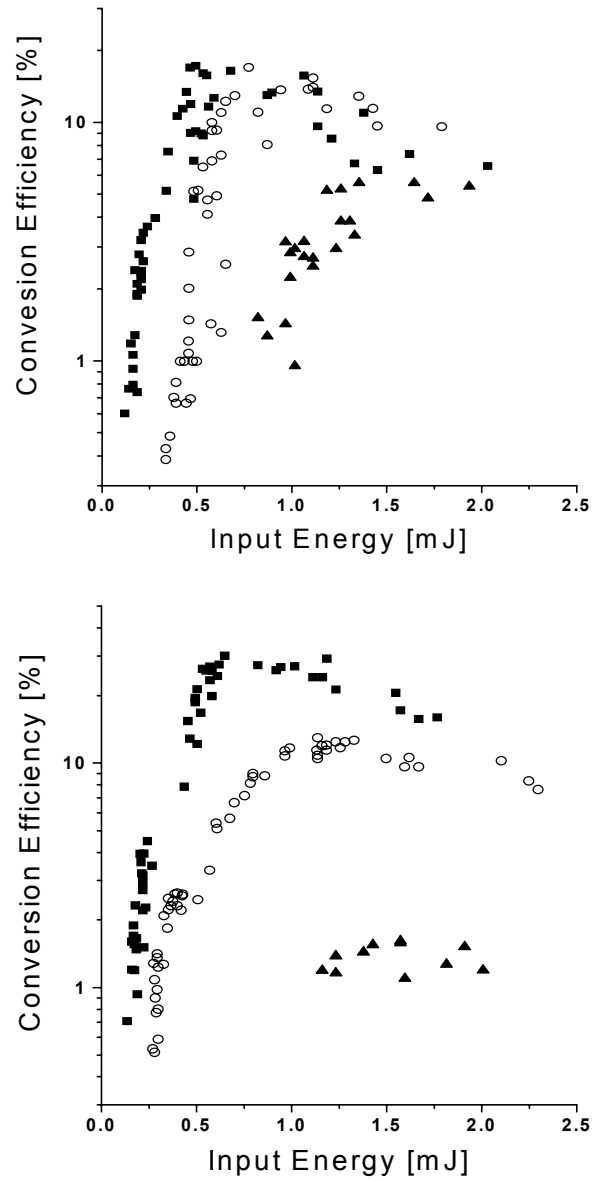| Crystal	Threshold Energy [mJ]		Experimental Picosecond Raman Gain [cm/GW]	Steady-state Raman Ggain [cm/GW]
	1st Stokes	2nd Stokes		
$BaWO_4$	0.14	0.24	14.4	36
$KGd(WO_4)_2$	0.14	0.30	11.5	16
$KY(WO_4)_2$	0.15	0.30	18.7	21
$Ba(NO_3)_2$			4.7 [4.4]	47 [4.1]

Fig. 4.8. Conversion efficiencies to the first (squares), second (circles), and third (triangles) Stokes

components as a function of pump energy ($\lambda = 532$ nm) for SRS in BaWO$_4$ (length 31 mm) and

KGd(WO$_4$)$_2$ (length 40 mm) crystals.

The threshold intensity values allowed us to calculate the experimental threshold gain coefficient $G_{exp}=25/I_P l$ to be equal to 14.4 cm/GW for BaWO$_4$, 11.5 cm/GW for KGd(WO$_4$)$_2$ and 18.7 cm/GW for KY(WO$_4$)$_2$ under 532-nm pumping (Table 4.5). Taking into account the vibronic relaxation time and the corresponding values of the transient gain coefficient F [4.6] the steady state Raman gain can be obtained to be 36 cm/GW, 16 cm/GW and 21 cm/GW for above crystals. So one can see that for 28 ps pump pulse duration the experimental Raman gain in BaWO$_4$ crystal is decreased 2.5 times from the steady state value but still remains higher than that in KGd(WO$_4$)$_2$ while in Ba(NO$_3$)$_2$ it is reduced 10 times and becomes much lower than in all tungstates. From these data we can predict even better performance of new BaWO$_4$ crystal compared with KGW for longer picosecond pump pulses 100-300 ps.

The Raman gain inversely depends on the square of the operating wavelength, which results in the lowering of the SRS efficiency at near IR 1064 nm fundamental wavelength compared with green 532 nm pumping. The measured threshold energies for this case are presented in Table 4.6. The values of the experimental Raman gain for 1064 nm pump wavelength were obtained to be 3.8 cm/GW for BaWO$_4$, 3.0 cm/GW for KGd(WO$_4$)$_2$ and 4.7

Table 4.6. The SRS threshold energies of the first and second Stokes components together with calculated Raman gains for BaWO$_4$, KGd(WO$_4$)$_2$ and KY(WO$_4$)$_2$ crystals with 1064 nm pump radiation.

Crystal	Threshold Energy [mJ]		Experimental Picosecond Raman Gain [cm/GW]	Steady-state Raman Gain [cm/GW]
	1st Stokes	2nd Stokes		
BaWO$_4$	2.32	3.07	3.8	8.5
KGd(WO$_4$)$_2$	2.28	3.8	3.0	3.5
KY(WO$_4$)$_2$	2.5	3.7	4.7	5.1

cm/GW for KY(WO$_4$)$_2$ (Table 4.6). This gave us the corresponding calculated values 8.5 cm/GW, 3.5 cm/GW and 5.1 cm/GW steady state Raman gains in the near IR. From Tables 4.5 and 4.6 it follows, that in spite of the fact that the integral Raman scattering cross section in BaWO$_4$ crystal is 20% less than that in KGW it shows the same or even lower threshold energy and Raman gain for picosecond regimes $t_p > 25$ ps, as well as for nanosecond. It becomes even more important if we take into account the difference in the transient behavior for $t_p = 25$ ps, where t_p / T$_2$ for BaWO$_4$ is less than for KGW. So we can outline this unique feature of our new BaWO$_4$ crystal as a universal for both pico- and nanosecond regimes of operation.

Maximum conversion efficiencies of the pump radiation to the first and second Stokes components were measured to be 30 % and 15% for BaWO$_4$ and 18% and 15% for KGd(WO$_4$)$_2$, respectively, without any additional Raman cavity. The conversion to the third Stokes component reached 2 % in BaWO$_4$ and 5 % in KGd(WO$_4$)$_2$. When scattering to the higher-order Stokes components appears, the saturation of the lower order Stokes was observed and their conversion efficiency was decreased. The higher SRS efficiency to the second and third Stokes components in case of KGd(WO$_4$)$_2$ crystal can be due to the longer length of this crystal.

The ability of the SRS to shorten laser pulses is well known and has found some practical applications. The temporal behaviour of the picosecond SRS radiation generated under self-SRS in Nd^{3+}:KGd(WO$_4$)$_2$ and Nd^{3+}:KY(WO$_4$)$_2$ laser was studied in details in Ref.[4.7]. Depending on laser energy, the Stokes pulses were reported to have two to three times shorter pulse duration comparing to pump pulse. The aim of our temporal pulse study was to measure the magnitude of laser pulse shortening that can be obtained by SRS in BaWO$_4$ crystal in our experimental arrangement. The obtained temporal profiles of the pump and the first Stokes pulses are presented in Fig. 4.9. The temporal length (FWHM) of the pump pulse and the first Stokes pulse was found to be 28 ps and 15 ps, respectively, for maximum pump energy. So one can conclude that the SRS in BaWO$_4$ leads to shortening of the Stokes pulse duration by a factor of about 2

comparing to pump pulse duration at pump energy approximately 3 times above the threshold level.
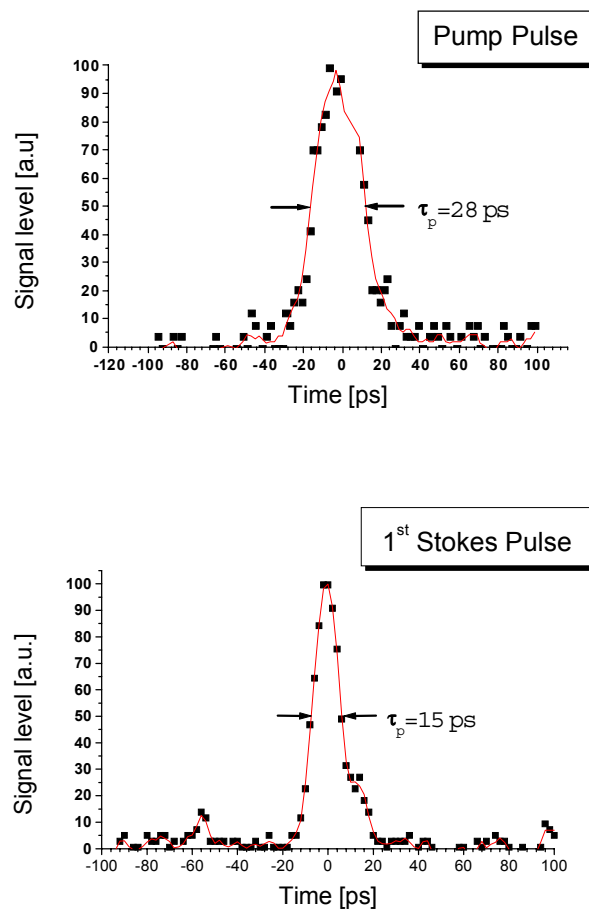

Fig. 4.9. Temporal pulse shape of laser 532 nm pump pulse and 1st Stokes pulse in BaWO$_4$.

Thus, our experimental study showed that newly developed $BaWO_4$ crystal is a very efficient solid state material for picosecond SRS. High value of its steady state Raman gain for nanosecond pulses is only twice reduced for 28 ps pump pulses but still remains higher than that in $KGd(WO_4)_2$ crystal and more than 3 times higher than in $Ba(NO_3)_2$. This is due to the fact that the linewidth of SRS-active line in $BaWO_4$ crystal is almost 4 times narrower than in $KGd(WO_4)_2$ crystal and equals 1.6 cm^{-1}. In case of homogeneous broadening this value corresponds to 6.6 ps vibronic relaxation time, which is longer than that for $KGd(WO_4)_2$ crystal - 1.9 ps. So for picosecond pulses with 25 ps pump pulse duration the transient behavior of SRS is not as important in $BaWO_4$ crystal as in $Ba(NO_3)_2$. This proves that barium tungstate can be considered as a unique crystal for wide variety of pump pulse duration from nanoseconds to picoseconds. The SRS in $BaWO_4$ crystal provides shortening of the pump pulse duration and can be used for the generation of the frequency shifted pulses with twice shorter pulse duration of about 15 ps.

Thus, our SRS threshold measurements have shown that $BaWO_4$ crystal has Raman gain coefficient of 36 cm/GW for green radiation (532 nm), 8.5 cm/GW for 1.064 μm, and about 6 cm/GW for 1.3 μm wavelength which is only 15% less than that in $Ba(NO_3)_2$. Due to better physical properties, $BaWO_4$ crystal is less fragile and non hydroscopic with better thermoconductivity, it could be perspective for development of powerful solid state Raman laser, SRS shifters and Raman amplifiers. It is necessary to note that $BaWO_4$ crystal exhibits also high value of integral cross section, typical for other tungstates. This makes this crystal highly efficient for picosecond, subnanosecond and nanosecond and longer pulse laser applications.

Our analysis and experimental data have shown that the cavity effect due to the reflection from the sample faces which can significantly reduce the SRS threshold is very important for Raman laser development.

4.3. SRS with cooled BaWO$_4$ Raman crystal

As we have seen above the estimated Raman gain for 1.3 µm pump wavelength should be less than 6 cm/GW. That's why special precautions should be made to reduce the SRS threshold in the near IR in order to obtain high conversion efficiency at pump intensities lower than the optical damage threshold. These precautions can include an additional cavity for Raman crystal, aligning crystal surfaces perpendicular to the pump beam axis. The SRS threshold can be reached easier by increasing the pump intensity without Raman crystal damage via shortening the pump pulse or by using picosecond pump pulses or nanosecond pulses with subnanosecond temporal structure.

Another possibility to increase the Raman gain and laser damage threshold is to cool the SRS crystal. The SRS experiments with cooled Raman crystal will be described in this chapter. The optical scheme of the experimental setup for SRS threshold measurements is presented in Fig. 4.10. It is similar to that described in the previous part of this chapter. To cool the BaWO$_4$ Raman crystal (6x6x40 mm) it was placed into the optical cryostat filled with liquid nitrogen. The sample was fixed at a cooper cold finger.

The energy and conversion efficiency dependencies of the first Stokes generation at 77K with different reflectivity output couplers under 1.064 µm nanosecond pumping ($t_p = 12$ ps) are shown in Figs. 4.11, 4.12. The maximal conversion efficiency (up to 40%) was obtained without any additional output mirror and used only the reflection from the crystal face as an output coupler. In this case the energy of 1.5 mJ were observed with 4 mJ pump pulse. From Figs. 4.11, 4.12 it follows that the optimal reflectivity of the SRS cavity output coupler is less than 25%. In this case ($R_{oc} = 25\%$) the SRS threshold is significantly reduced, while the conversion efficiency is higher than 20%. The slope efficiency for SRS generation was higher than 80% in these measurements and close to physical limit.
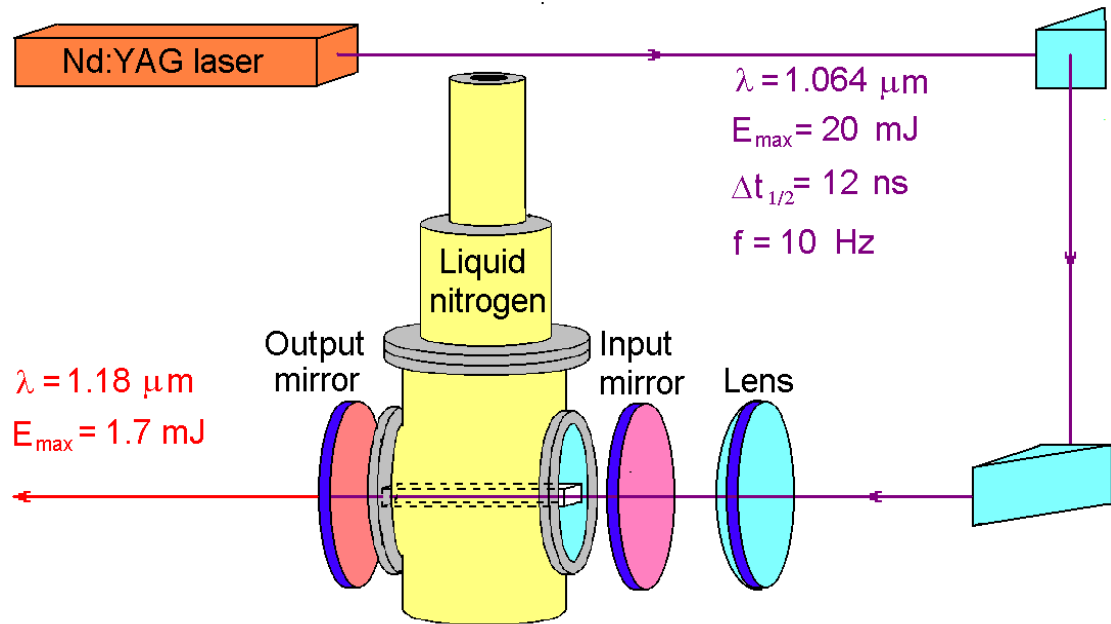
Nd:YAG laser

λ = 1.064 μm

E_{max}= 20 mJ

$\Delta t_{1/2}$= 12 ns

f = 10 Hz

Liquid nitrogen

Output mirror

Input mirror

Lens

λ = 1.18 μm

E_{max} = 1.7 mJ

Fig. 4.10. Experimental setup for SRS threshold measurements in BaWO$_4$ crystal at
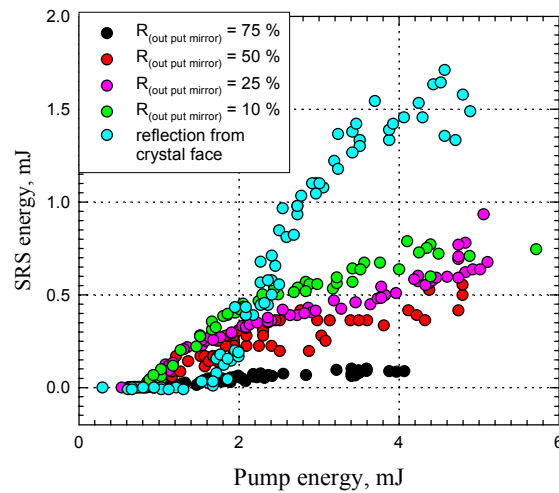
77K with 1064 nm wavelength pumping.

Fig. 4.11. Dependencies of the first Stokes component energy (λ = 1.18 µm) in BaWO$_4$ Raman laser on the pump energy (λ = 1.064 µm) at 77 K temperature for output couplers with different reflectivity at 1.18 µm (75%, 50%, 25%, 10% and without additional mirror).
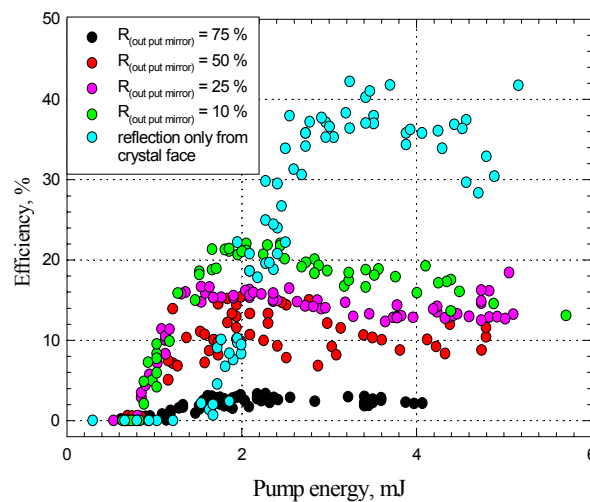

Fig.4.12. Dependencies of the BaWO$_4$ Raman laser conversion efficiency to the first Stokes component (λ = 1.18 µm) on the pump energy (λ = 1.064 µm) at 77 K for output couplers with different reflectivity at 1.18 µm (75%, 50%, 25%, 10% and without additional mirror).

In the second set of experiments the pump laser with 1318 nm output radiation was used. It was a pulsed-periodic (f = 3 Hz) multimode Nd^{3+}:YAG laser with acousto-optical Q-switching. It provided the pump pulses with 1318 nm wavelength, energy up to 20 mJ and pulse duration of about 50 ns. The experimental setup is presented in Fig. 4.13. The pump radiation was focused inside barium tungstate sample with the lens 15 cm focal length. The pump energy at the entrance of the Raman crystal was smoothly reduced by various neutral density filters. To measure the pump energy, part of it was reflected by a glass plate to a photodiode. The collimated Stokes radiation was spectrally selected by dichroic mirror. The scattered energy was measured with a photodiode calibrated with energy meter. The scattered and pump beams were measured simultaneously by the digital oscilloscope Tektronix TDS-380. Due to the fluctuation of the pump energy the intensity of the scattered Stokes radiation changed from pulse to pulse. The registration system allowed to make the single pulse measurements which increased the accuracy of SRS measurements. The barium tungstate crystal (40 mm long) was placed into additional cavity composed by entrance mirror ($R_{1.318}$ = 18%, $R_{1.50} \approx 100\%$) and output coupler with variable reflectivity ($R_{1.50}$ = vary).

Figs. 4.14 and 4.15 present the results on the first Stokes component energy in the Raman laser output and conversion efficiency for two crystal temperatures in the same optical setup with 17% reflectivity output coupler. The maximal 1st Stokes energy reached 1.8 mJ with conversion efficiency 12% at pump energy of 14 mJ. The fitted lines show that the SRS threshold was slightly less for 77K crystal temperature than for 300K. The conversion efficiency at lower pump energy was slightly higher for 77K. However the maximal energy (2.0 mJ) and conversion efficiency (15%) were obtained at room temperature with 10-12 mJ pump pulses. This lower values at 77 K can be due to the imperfections of the cryostat cell that has windows without antireflection coatings.
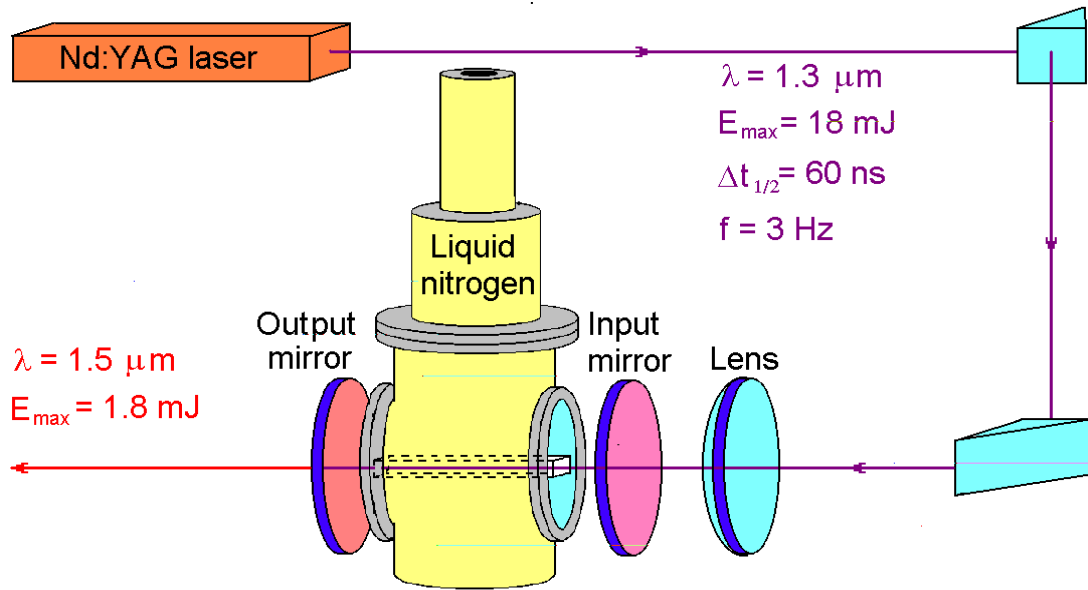
Fig. 4.13. Experimental setup for SRS experiments in BaWO$_4$ Raman laser at 77K with 1320 nm pump wavelength.
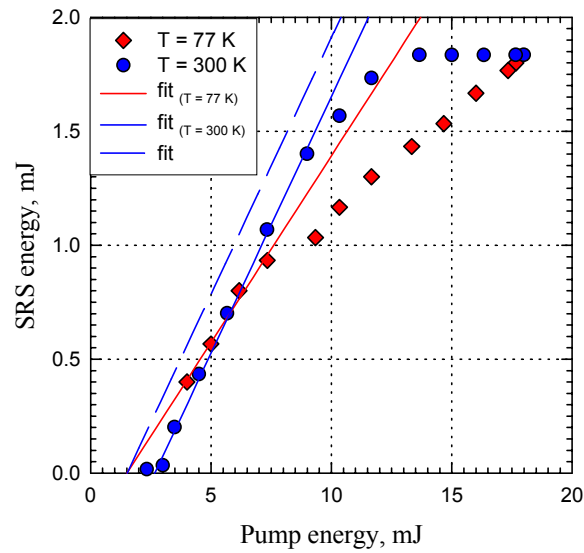
Fig. 4.14. Dependencies of the BaWO$_4$ Raman laser energy in the first Stokes component ($\lambda = 1.50\ \mu m$) on the pump energy ($\lambda = 1.318\ \mu m$) for two crystal temperatures 77 and 300K temperatures with R$_{1.50}$ = 17% reflectivity output coupler.
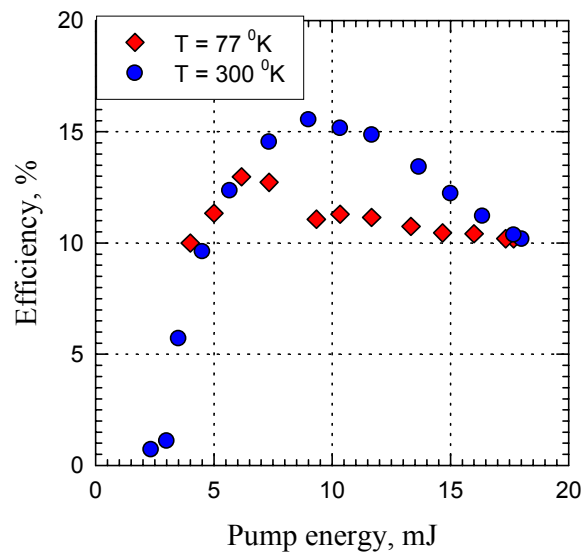

Fig. 4.15. Dependencies of BaWO$_4$ Raman laser conversion efficiency to the first Stokes component ($\lambda = 1.50\ \mu m$) on the pump energy ($\lambda = 1.3\ \mu m$) for two crystal temperatures 77 and 300 K and with R$_{1.50}$ = 17% reflectivity output coupler.

The results on the investigation of SRS at 77K crystal temperature versus the output coupler reflectivity are shown in Figs. 4.16, 4.17. The experimental energy dependencies of the 1st Stokes Raman laser output energy and conversion efficiency for 1.3 μm pump laser with 17% reflectivity output coupler and without any additional output mirror are presented in Figs. 4.16, 4.17. Similar to 1.06 μm pumping higher efficiency was observed when only the reflectivity from crystal face worked as an output coupler. In this case the reflectivity from the crystal surface was aligned perpendicular to the Raman cavity axis. The SRS energy increased up to 3 mJ and conversion efficiency was as high as 19% when pumped with 18 mJ pulses. One can see that the real SRS conversion efficiency in BaWO$_4$ crystal in the external cavity was measured to be up to 20% with the slope efficiency higher than 35%. No saturation was observed in the behavior of this dependence and the further increase of the pump energy can result in the consequent increase of the conversion efficiency.
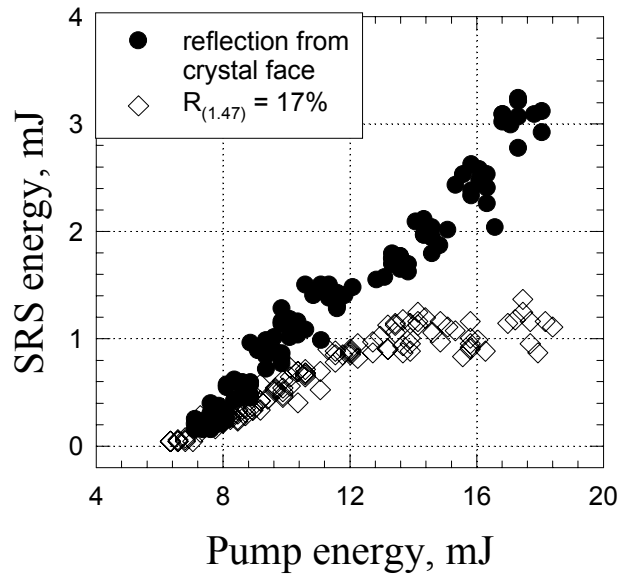
Fig. 4.16. The dependencies of the BaWO$_4$ Raman laser output energy in the 1st Stokes component (λ_R = 1.50 μm) vs. pump energy (λ_P = 1.318 μm) at 77K crystal temperature with 17% reflectivity output coupler mirror and only with reflection from the crystal face.

Fig. 4.17. The dependencies of the BaWO$_4$ Raman laser conversion efficiency to the 1st Stokes component (λ_R = 1.50 μm) vs. pump energy (λ_P = 1.318 μm) at 77 K crystal temperature with 17% reflectivity output coupler mirror and only with reflection from the crystal face.
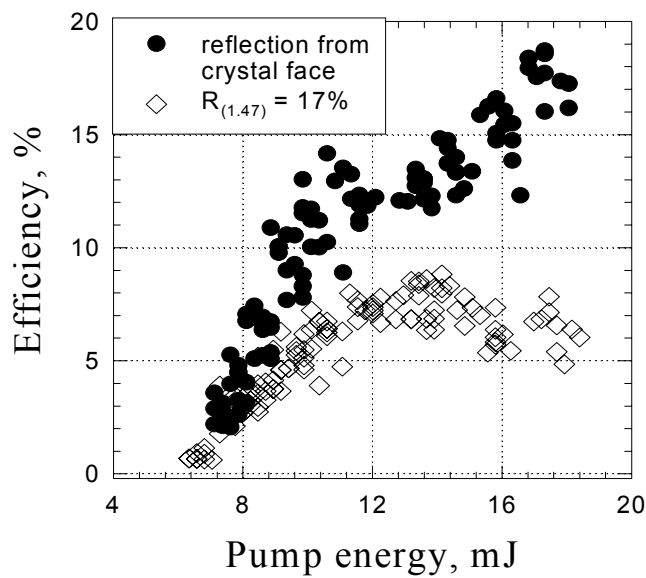
References to chapter 4:

4.1.   P.G. Zverev, T. T. Basiev, and A. M. Prokhorov, «Stimulated Raman scattering of laser radiation in Raman crystals», Optical Materials, vol. **11,** 335-352 (1998).

4.2.   A. S. Eremenko, S.N. Karpukhin, and A.I. Stepanov, "SRS of second harmonic of neodymium laser in nitrate crystals," Sov. J. Quantum Electron., **10,** 113 (1980).

4.3.   T. T. Basiev, V. N. Voitsekhovskii, P. G. Zverev, F. V. Karpushko, A. V. Lubimov, S. B. Mirov, V. P. Morozov, I. V. Mochalov, A. A. Pavlyuk, G. V. Sinitsyn, and V. E. Yakobson, "Conversion of tunable radiation from a laser utilizing LiF crystal containing F_2^- color centers by stimulated Raman scattering in $Ba(NO_3)_2$ and $KGd(WO_4)_2$ crystals," Sov. J. Quantum Electron., **17,** 1560 (1987).

4.4.   P. G. Zverev, J. T. Murray, R. C. Powell, R. J. Reeves and T. T. Basiev, "Stimulated Raman scattering of picosecond pulses in barium nitrate crystals", *Opt. Commun*. **97** (1993) 59-64.

4.5.   T. T. Basiev, M. E. Doroshenko, P. G. Zverev, H. Jelinkova, "Efficient Raman shifting of picosecond Nd:YAG radiation by KGW crystal", Technical Digest of Conference on Lasers and Electro-Optics, *OSA Technical Digest Series*, **6** (1998) 257.

4.6.   R. L. Carman, F. Shimizu, C. S. Wang, and N. Bloembergen, "Theory of Stokes pulse shapes in transient stimulated Raman scattering," *Phys. Rev. A* **2**, 60-72 (1972). Y. Wang, "Theory of stimulated Raman scattering," *Phys. Rev.* **182**, 482-494 (1969).

4.7.   K. Andryunas, Yu. Vishchakas, V. Kabelka, I. A. Mochalov, A. A. Pavlyuk, G. T. Petrovskii, and V. Syrus, "Self-SRS conversion of Nd^{3+} ; laser emission in crystals of double tungstates," Letters to J. Experimental and Theoretic Physics, *Zh. Eksp. Teor. Fiz. Pis'ma Red.* **42**, 333-365 (1985).

5. Thermal Properties of SRS

5.1. Development of AC calorimetry technique for measuring thermal conductivity in solids

Introduction

AC calorimetry is a powerful technique, which was successfully used for time-dependent or frequency-dependent heat capacity and thermal conductivity measurements in condensed matter systems [5.1 - 5.13].

Recently, the new capabilities of AC calorimetry, when working at frequencies above classical limit, were demonstrated [5.12, 5.13]. The advanced AC calorimetry was developed on the basis of the classical AC calorimetry technique. The idea of the method was to use the information about the phase and the amplitude of the temperature wave transmitted through a plate-like sample for simultaneous determination of the sample's heat capacity C_s and thermal conductivity κ_s. It was shown, that the AC calorimeter, described in [5.14, 5.15], can be used at relatively high frequencies, when the temperature oscillations in the sample are not quasi-static. In this calorimeter an oscillating heat flow $P_0 \cdot \cos(\omega t)$ is supplied to one side of the sample, and the temperature oscillations $T_0 \cdot \sin(\omega t + \varphi)$ are measured on the other side. The two parameters, C_s and κ_s, can be determined from the two measured values, the amplitude T_0 and the phase φ of the transmitted temperature wave. The mathematical algorithm to do so was described in the paper [5.12]. More over, using the information about the amplitudes T_{01} and T_{02} as well as the phases φ_1 and φ_2 on both sides of the sample, one can obtain *simultaneously* the complex heat capacity $C_s(\omega)$ and the complex thermal conductivity $\kappa_s(\omega)$, i.e. four parameters: $Re(C_s)$, $Im(C_s)$, $Re(\kappa_s)$ and $Im(\kappa_s)$. Thus, the improvement of classical AC calorimetry has brought up a novel method. Its physical mechanism is transmission of temperature waves through a sample.

The advanced AC calorimetry was successfully applied to studies of polymer materials

where the ideal thermal contact of the sample with the calorimeter cell was assumed [5.12, 5.13]. This approximation was sufficient for polymers – the materials with relatively low thermal conductivity. Usually, after first melting-crystallization cycle polymers provide a good and stable thermal contact due to nice adhesion with substrate. On the other hand, the thermal contact should be wet in the case, when the sample can not be melted. The thermal conductance of the dry thermal contact is very low and irreproducible. This conductance depends on the ambient gas pressure as well as on the sample-to-substrate pressure. Thus, when dealing with solids, a good «wet» contact can be made by forming a thin layer of some adhesive surfactant between the sample and substrate. The vacuum grease, apiezon, can be used for a good thermal contact. The grease layer can be made with reproducible thickens. Furthermore, the relatively small temperature gradient in the thin grease layer can be neglected, provided a sample with low thermal conductivity, $\kappa_s < 1$W/m·K, is investigated. Nevertheless, this approximation can not be applied for materials with higher thermal conductivity.

Below we will describe the further developments of AC technique, taking into account the thermal contact conductance on the sample's faces. To focus on the thermal contact conductance, we consider only the case of the frequency independent sample's parameters C_s and κ_s. To determine the parameters C_s and κ_s simultaneously, it is sufficient to measure temperature modulation on that side of the sample, which is opposite to the heated sample's surface. It is noteworthy, that the method can be applied for the case of complex sample's parameters, provided temperature modulation amplitudes are measured on both sides of the sample.

In the next section we present the description of the physical principles of the method and the mathematical algorithm of C_s and κ_s calculations from the measured complex amplitude of the temperature modulation. The calibration of the calorimeter and the thermal contact conductance is described in the third part. The fourth paragraph is devoted to the experimental

investigation of the thermal contact reproducibility and the measurements linearity relative to the sample's thickness. In the fifth section we will present the experimental results for materials with different thermal conductivity and estimate the accuracy of this technique. The last paragraph presents results on the investigation of the thermal conductivity of KGW Raman crystal.

Description of the method

The calorimeter cell – the system for creation and registration of temperature modulation in a disk-shaped sample – consists of a heater, a sensor, and a holder. The sample is placed between the heater and the sensor substrates. Thin layers of vacuum grease (apiezon) are used for providing good thermal contacts at the sample's faces. The heater and the sensor are formed on the surfaces of polished sapphire disks of 3.0 mm diameter and of thickness 100 μm. The heater is a chromium film of about 0.1 μm, sputtered on the first sapphire substrate. Copper contact pads are sputtered on the film, and copper wires of 50 μm diameter are welded to the pads. The power of the resistive heater equals $P_0 \cdot (1 + \cos\omega t)$, where $\omega/2$ is the angular frequency of the electric current and P_0 is the average power of the heater. To form the sensor, a copper field is sputtered on the second sapphire substrate. The thermocouple (Cu–Cu:Fe) wires of 50μm diameter are welded to the copper field. The sensor is glued on a silk net, which serves as holder. Thus, the system consists of six layers, including sample and two grease layers.

This layered system is heated by uniform heat flow of oscillating rate $P = P_0 \cdot \cos(\omega t)$. The flow is applied to the outer face of the first layer at $z = 0$ and propagates through the system along z-axis. The cross area S of the system is independent on z. Provided the heat leakage through the perimeter of the system is negligible, the plane temperature waves $T = \text{Re}[T_0 \cdot \exp(i\omega t \pm \mathbf{k}z)]$ propagate across the system, where $\mathbf{k} = \exp(i\pi/4) \cdot (\omega c/\kappa)^{1/2}$, c – specific heat capacity and κ – thermal conductivity of the material. In other words $\mathbf{k} = (k + i \cdot k)/\sqrt{2}$, where $k = (\omega c/\kappa)^{1/2}$.

Thus, the wave number and the damping coefficient of these waves are equal to $k/\sqrt{2}$. Stationary oscillating solution of the heat transfer equation without heat sources can be written as follows: $\mathrm{Re}\{\exp(i\omega t)\cdot[\mathbf{a}\cdot\sinh(\mathbf{k}z) + \mathbf{b}\cdot\cosh(\mathbf{k}z)]\}$. Therefore the temperature wave $\mathbf{T}_i(z)=\exp(i\omega t)\{\mathbf{a}_i\cdot\sinh[\mathbf{k}_i(z - \xi_i)] + \mathbf{b}_i\cdot\cosh[\mathbf{k}_i(z - \xi_i)]\}$ is excited in i-th layer, where ξ_i is the coordinate of i-th boundary. The complex coefficients $\mathbf{a}_i$ and $\mathbf{b}_i$ are determined by boundary conditions for temperature and heat flow amplitudes on faces of i-th layer. The amplitude and the phase of the temperature wave propagating through the sample is measured. The complex amplitude $\mathbf{T}_A$ of the temperature modulation is measured on the surface between the sensor and the holder in the calorimeter considered in this paper.

In general, the following effective heat capacity is measured in classical AC calorimetry:

$$\mathbf{C}_{\mathrm{eff}} = P_0 /(i\omega\mathbf{T}_A), \tag{5.1}$$

which is proportional to the heat-flow amplitude P_0 and inversely proportional to the measured complex amplitude $\mathbf{T}_A$. Of course, at sufficiently low frequencies and sufficiently low heat-link between the system and the thermostat the effective heat capacity $\mathbf{C}_{\mathrm{eff}}$ equals the sum of the sample's heat capacity C_s and the heat capacity of the empty cell. The phase shift $\varphi = -\mathrm{Arg}$ ($\mathbf{C}_{\mathrm{eff}}$) between the temperature modulations in the heater and in the sensor equals zero at these conditions. In fact, the phase shift between the heat-flow and $\mathbf{T}_A$ equals $\varphi - \pi/2$. As the trivial phase $\tanh(\pi/2)$ is not of interest, we consider the phase shift φ between temperature modulations on the opposite sides of the system. At higher frequencies the relation between the measured $\mathbf{C}_{\mathrm{eff}}$ and C_s is complicated.

As it was shown in [5.12], provided the heat leakage into the wires of the thermocouple and through the perimeter of the system is negligible, the measured $\mathbf{C}_{\mathrm{eff}}$ for the system consisting of n layers can be expressed as follows:

$$\mathbf{C}_{\mathrm{eff}} = \cosh(\alpha_1)...\cosh(\alpha_{n-1})\cdot[C_1\cdot\tanh(\alpha_1)/\alpha_1 +...+ C_n\cdot\tanh(\alpha_n)/\alpha_n + G / i\omega + \mathbf{B}] , \tag{5.2}$$

where $\alpha_i = \exp(i\pi/4)a_i$, $a_i = d_i\cdot k_i$ – the parameter characterizing the thermal length of the i-th

layer, d_i is the thickness of the i-th layer, C_i – heat capacity of the i-th layer, G – ambient gas depending constant, characterizing the heat-link between the system and the thermostat. The cross terms are presented by the sum $\mathbf{B} = \mathbf{B}_3 + \mathbf{B}_5 + ... + \mathbf{B}_{2m+1}$, where $2m+1 \le n$. Denote $\beta_{ab} = \kappa_a k_a / \kappa_b k_b$, then $\mathbf{B}_i$ can be written as follows:

$$\mathbf{B}_3 = \sum (C_a/\alpha_a) \cdot \beta_{cb} \cdot \tanh(\alpha_a) \cdot \tanh(\alpha_b) \cdot \tanh(\alpha_c), \tag{5.3}$$

$$\mathbf{B}_5 = \sum (C_a/\alpha_a) \cdot \beta_{cb} \cdot \beta_{ed} \cdot \tanh(\alpha_a) \cdot \tanh(\alpha_b) \cdot \tanh(\alpha_c) \cdot \tanh(\alpha_d) \cdot \tanh(\alpha_e),$$

and so on for all indexes, such as a<b<c<d<e... . The sum $\mathbf{B}_3$ is taken over all combinations of three elements from n, i.e. over C_n^3 elements, $\mathbf{B}_5$ - over all combinations of five elements from n, over C_n^5 elements, and so on. The cross terms are negligibly small at sufficiently low frequencies. Indeed, $\tanh(\alpha_i) \approx \alpha_i$ at small α_i, and α_i decrease with frequency as $\alpha_i \sim \sqrt{\omega}$. Noteworthy, that the Eq.(5.2) was obtained in general case, when the sample's heat capacity and thermal conductivity can be complex.

Consider the Heater-Sample-Sensor-Holder system consisting of six layers, including two grease layers between sample and heater as well as between sample and sensor. Note that the heater and the sensor are formed on the equal sapphire substrates. That is why, we denote C_0 and d_0 – the total heat capacity and the total thickness of two substrates, c_0 and κ_0 – specific heat capacity and thermal conductivity of sapphire. Denote the parameters of the holder and of the grease layer in the same manner with subscripts h and g. In the case of six layers, at n=6, the sum $\mathbf{B}$ in Eq.(5.2) equals $\mathbf{B}_3 + \mathbf{B}_5$, where $\mathbf{B}_3$ is the sum of 20 elements, and $\mathbf{B}_5$ is the sum of 6 elements. The Eqs. (5.2) and (5.3) can be simplified, if we take into account that the grease layer is relatively thin, d_g ca.4μm, and $C_g \ll C_0$. Thus, the terms from $\mathbf{B}_3$, which are proportional to β_{gi}, can be neglected, because $\alpha_g \cdot \beta_{gi}$ proportional to C_g. On the other hand, the terms from $\mathbf{B}_3$, which are proportional to β_{ig}, can not be neglected. Note, that $\alpha_g \cdot \beta_{ig} = (i\omega \cdot C_i)/(K_g \cdot \alpha_i)$, where $K_g = S \cdot \kappa_g/d_g$ – the thermal conductance of the grease layer. Denote $K_0 = S \cdot \kappa$

$_0/d_0$ – the thermal conductance of the sapphire substrates, $\tau_g = C_0/K_g$ and $\tau_0 = C_0/K_0$ – the characteristic times of thermal relaxation in the system. In fact, at room temperatures τ_g ca.10^{-2}s and τ_0 ca. $5 \cdot 10^{-3}$s. Thus, $\tau_g > \tau_0$ in spite of small thickness d_g.

Consider Eqs.(5.2) and (5.3) at modulation frequency $f = \omega/2\pi$ below 100Hz, when $\alpha_g \ll 1$ and $\tanh(\alpha_g) \approx \alpha_g$. In this case, the cross terms from $\mathbf{B_5}$ can be neglected within 4% accuracy. In fact, the main term in the sum $\mathbf{B_5}$ is $(C_0/\alpha_0) \cdot \beta_{sg} \cdot \beta_{h0} \cdot \tanh(\alpha_s) \cdot \tanh(\alpha_g) \cdot \tanh(\alpha_h) \cdot [\tanh(\alpha_0/2)]^2$, which is equal to $\boldsymbol{\varepsilon} \cdot [C_s \cdot \tanh(\alpha_s)/\alpha_s]$, where $\boldsymbol{\varepsilon} = (i\omega\tau_g) \cdot (i\omega\tau_0) \cdot (C_h/C_0) \cdot [\tanh(\alpha_h)/\alpha_h] \cdot [\tanh(\alpha_0/2)/\alpha_0]^2$ and $\boldsymbol{\varepsilon} \ll 1$. Actually, this term can be neglected at any temperatures and frequencies below 100Hz, provided the error ca. 4% is acceptable. Thus, only the cross terms from $\mathbf{B_3}$ are taken into account. Consider the cross terms $(C_a/\alpha_a) \cdot \beta_{cg} \cdot \tanh(\alpha_a) \cdot \tanh(\alpha_g) \cdot \tanh(\alpha_c)$, which can not be neglected. These terms can be written as follows: $(i\omega/K_g) \cdot [C_a \cdot \tanh(\alpha_a)/\alpha_a] \cdot [C_c \cdot \tanh(\alpha_c)/\alpha_c]$. Then, the effective heat capacity for the Heater-Sample-Sensor-Holder system at modulation frequencies below 100Hz can be expressed as follows:

$$\mathbf{C_{eff}} = \cosh(\alpha_0) \cdot \cosh(\alpha_s) \cdot \cosh(\nu\alpha_g) \cdot [\mathbf{A_0} + \mathbf{A_h} + \nu C_g + G/i\omega + \mathbf{S_0} + \mathbf{S_h}], \qquad (5.4)$$

$$\mathbf{A_0} = [C_0 \cdot \tanh(\alpha_0)/\alpha_0] \cdot [1 + (i\omega\nu\tau_g) \cdot \tanh(\alpha_0/2)/\alpha_0],$$

$$\mathbf{A_h} = [C_h \cdot \tanh(\alpha_h)/\alpha_h] \cdot [1 + (i\omega\nu\tau_g) \cdot \tanh(\alpha_0)/\alpha_0],$$

$$\mathbf{S_0} = [C_s \cdot \tanh(\alpha_s)/\alpha_s] \cdot \{1 + (i\omega\nu\tau_g) \cdot \tanh(\alpha_0)/\alpha_0 + [(\beta_{0s})^2 - 1] \cdot [\sinh(\alpha_0/2)]^2/\cosh(\alpha_0)\},$$

$$\mathbf{S_h} = [C_h \cdot \tanh(\alpha_h)/\alpha_h] \cdot [(i\omega\nu\tau_{sg}) \cdot \tanh(\alpha_s)/\alpha_s + (\beta_{0s}/2 + \beta_{s0}/2) \cdot \tanh(\alpha_0) \cdot \tanh(\alpha_s)],$$

where $\tau_{sg} = C_s/K_g$, $\nu = 2$ is the number of grease layers, $\beta_{s0} = 1/\beta_{0s}$ and $\beta_{0s} = (C_0 \cdot \alpha_s)/(C_s \cdot \alpha_0)$ by definition. Of course, the obvious relation $\mathbf{C_{eff}} \approx (C_0 + C_h + 2C_g + C_s + G/i\omega)$ follows from Eq.(5.4) at sufficiently low frequencies. In general, the two parameters C_s and α_s can be determined from the measured complex $\mathbf{C_{eff}}$, provided other parameters in Eq.(5.4) are known. Finally, the thermal conductivity κ_s is determined from the following relation: $\kappa_s = \omega \cdot C_s \cdot d_s/S \cdot \alpha_s^2$.

Calibration of the calorimeter

Consider the effective heat capacity $\mathbf{C}_{emp}$ of the empty cell consisting of four layers. The expression for $\mathbf{C}_{emp}$ follows from Eq.(5.4) at $C_s=0$, $\alpha_s=0$ and $\nu=1$:

$$\mathbf{C}_{emp} = \cosh(\alpha_0)\cdot\cosh(\alpha_g)\cdot[\mathbf{A}_0 + \mathbf{A}_h + C_g + G/i\omega], \qquad (5.5)$$

This is only the parameter G which depends on ambient gas pressure. But this dependence is very weak in the pressure range 1-100 Pa. In all measurements the nitrogen gas pressure was about 10 Pa and G was equal to 1.07 mW/K at 300K. The cell parameters G, $\alpha_0/\sqrt{f}$, $\alpha_h/\sqrt{f}$, C_0, C_h, was determined in advance without a sample. The parameters of the grease layer, $\alpha_g/\sqrt{f}$, K_g and C_g, are related to the dimensionless parameter p, characterizing the thickness of the layer. This thickness was reproducible within 10% accuracy, with the average value $p_0 = 1$, corresponding to the average thickness about 4 μm. The parameters of the average grease layer were determined from the measurements for the multi-layered system with three equivalent sapphire samples and four grease layers. It was found, that $K_g = (1/p)\cdot 0.27$ W/K, $\alpha_g/\sqrt{f} = p\cdot 0.051$ s$^{1/2}$ and $C_g = p\cdot 0.07$ mJ/K at 300K.

Thus, we have six parameters for fitting the experimental dependence $\mathbf{C}_{emp}(T, f)$ by Eq.(5.5) at any fixed temperature in the broad frequency range 0.1-100Hz. The experimental dependencies of the absolute value $C_{emp}(300K,f)$ and the phase shift $\varphi = -\,\text{Arg}(\mathbf{C}_{emp})$ for a normal and a relatively thin grease layers are shown in Fig. 5.1. These experimental curves are well described by Eq.(5.5) in the frequency range 0.1-100Hz at the following parameters: C_0=4.3mJ/K, C_h=2.05mJ/K, $\alpha_0/\sqrt{f}$ =0.17s$^{1/2}$, $\alpha_h/\sqrt{f}$ =2.19s$^{1/2}$, G=1.07mW/K with p=0.95 for the first curve and p=0.7 for the second. To illustrate the influence of the thermal contact conductance, the curves, calculated for the ideal thermal contact (p = 0), are shown by dashed lines. As shown in Fig. 5.1, the thermal contact conductance has no effect on $C_{emp}(300K,f)$ at frequencies below 10Hz, but this effect is essential at ca. 100Hz.

Once the cell calibration is performed, the described algorithm makes it possible to carry out

simultaneous measurements of the sample's heat capacity and thermal conductivity. The measurements of C_{eff} vs frequency were performed at constant heat-flow amplitude P_0. Depending on the sample's heat capacity, P_0 was varied in the range $6 - 20$ mW so as the temperature-modulation amplitude T_A to be approximately the same for samples with different mass. Indeed, the amplitude T_A was decreased with frequency at constant P_0. In all experiments the amplitude T_A was changed in the range from 2K to 10^{-3}K with frequency variation in the range $0.1 - 100$Hz.
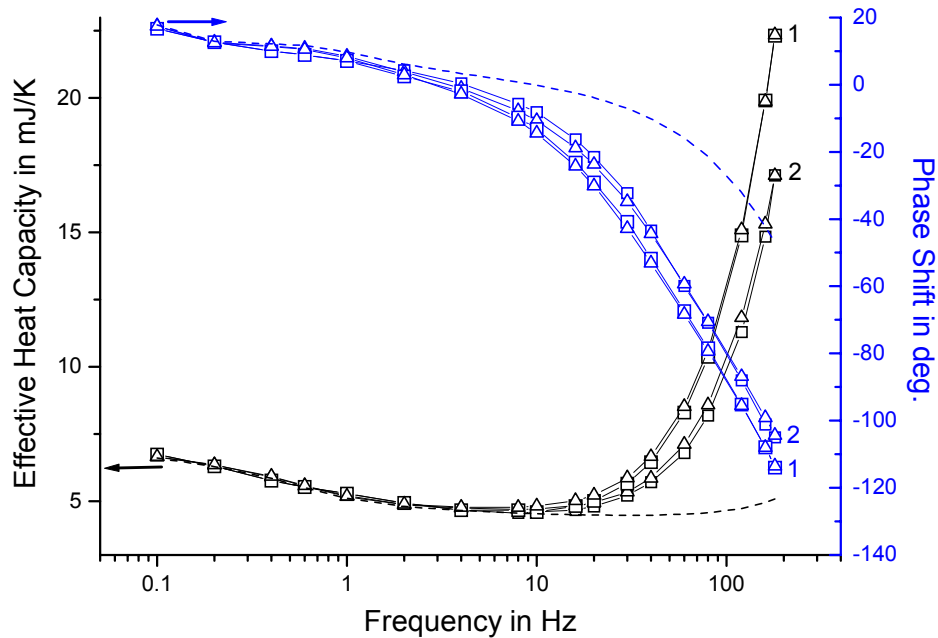
Fig. 5.1. Frequency dependencies of measured (squares) and calculated (triangles) effective heat capacity $C_{emp}(300K)$ and phase shift $\varphi = - Arg(C_{emp})$ for empty cell; 1 - for the normal grease layer with the thickness parameter $p = 0.95$ and 2 – for relatively thin layer with $p = 0.7$. The dashed lines show the dependencies for the ideal thermal contact with $p = 0$.

Thermal contact reproducibility and measurements linearity

Further, we check the reproducibility of the thermal contact conductance and of the measurements linearity relative to the sample's thickness. Consider the results obtained for a set of identical samples. The samples, received from «Kristallhandel Keplin» company, were polished sapphire disks of 5.0 mm diameter and of thickness $d_s = 110$ μm. The disks were cut out in C-plane of sapphire single crystal. All parameters of these disks were the same as of the cell-substrates, except thickness. Note, that the thickness of one cell-substrate equals $d_0/2 = 100$ μm. Therefore, the sample's parameters were known from the previous measurements: $C_s = 0.55 \cdot C_0$ and $\alpha_s/\sqrt{f} = 0.55 \cdot \alpha_0/\sqrt{f}$.

These parameters correspond to the specific heat capacity $c_s = (3.0 \pm 0.05) \cdot 10^6$ J/m$^3 \cdot$K and the thermal conductivity $\kappa_s = (27 \pm 1)$ W/m·K. The specific heat capacity is in agreement with the data available in the Web page [5.16]: $c = 750$ J/kg·K and density $\rho = 3985$ kg/m^3, i.e. $c = 2.99 \cdot 10^6$ J/m$^3 \cdot$K. The thermal conductivity $\kappa_s = 27$ W/m·K is smaller than the value $\kappa = 35 - 40$ W/m·K, which is presented in [5.16] for a bulk sapphire crystal of a purity 99.9%. Our result, obtained for the thin sapphire substrates, are in agreement with the data presented in [5.17] for the analogous thin sample: $\kappa = 25.1$ W/m·K, $d = 100$μm. Due to mechanical treatment, the sample structure is disturbed near the polished faces. The disturbed layers near the surfaces of a thin disk can be responsible for this relatively small thermal conductance. Another explanation is that the samples was not so pure. Nevertheless, the parameters of the all samples in the following experiment were the same.

The experimental dependencies of $C_{eff}(300K,f)$ and the phase shift $\varphi = - \text{Arg}(\mathbf{C}_{eff})$ for one, two and three sapphire samples as well for the empty cell are shown in Fig. 5.2. These experimental curves are well described by Eq.(5.4) in the frequency range $0.1 - 100$Hz with the following parameters: $C_s = n \cdot (d_s/d_0) \cdot C_0$, $\alpha_s = n \cdot (d_s/d_0) \cdot \alpha_0$ and $\nu = n + 1$, where $n = 0, 1, 2, 3$ is the number of sapphire samples in the cell, ν – the number of the grease layers. The grease

thickness parameter p was as follows: p = 0.95 for the empty cell, p = 1.00 for one sapphire sample, p = 1.10 for two samples and p = 1.01 for three samples. Thus, the grease layer thickness is reproducible within 10% accuracy. It is shown, that the experimental results for sapphire thermal parameters, c_s and κ, are independent on the number of samples in the cell, that is on the sample's thickness.

Experimental results for various materials and accuracy

Once the thermal contact conductance is taken into account, the thermal parameters of materials with relatively high thermal conductivity can be measured. Consider the experimental results for a copper monocrystalline sample. The sample was the polished disk of 3.1mm diameter and 500μm thickness. The frequency dependencies of measured and calculated effective heat capacity C_{eff}(300K) and of the phase shift $\varphi = -\ Arg(\mathbf{C}_{eff})$ for this sample are shown in Fig. 5.3. The experimental curves are well described by Eq.(5.4) in the frequency range 0.1-100Hz at the following parameters: C_s=12.9 mJ/K, $\alpha_s/\sqrt{f}$ =0.113 $s^{1/2}$ and p = 1.15. These results correspond to the following sample's parameters: $c_s = (3.4 \pm 0.05)\cdot10^6$ J/m$^3\cdot$K and $\kappa_s = 420 \pm 20$ W/m·K. This values are in agreement with the data available in the Web page [5.16]: $\kappa = 401$ W/m·K, density $\rho = 8960$ kg/m^3 and c = 385 J/kg·K, i.e. c = 3.45·10^6 J/m^3·K.

The relative error of the effective heat capacity fitting, $\delta C_{eff} = \Delta C_{eff}/C_{eff}$, and the absolute error of the phase shift fitting, $\Delta\varphi$, are shown in the insert of Fig. 5.3. The increase of the errors δC_{eff} and $\Delta\varphi$ with the frequency can be attributed to that fact, that the cross terms from the sum B_5 were neglected. The fluctuations of the measured $\mathbf{C}_{eff}$ around the mean value are increased with the frequency also. This growth of the fluctuations is attributed to the reduction of T_A and of the measured signal with the frequency at constant P_0. It is noteworthy, that the parameter C_s can be determined from the low-frequency part of C_{eff}(f) dependence directly, where the error δ $C_{eff} < 2\%$. On the other hand, the parameter $\alpha_s/\sqrt{f}$ is determined from the high-frequency part of

the curves, where the error in the curves fitting reaches 5%. Therefore, the heat capacity C_s is determined within 2% accuracy and the thermal conductivity κ_s within 5% accuracy.
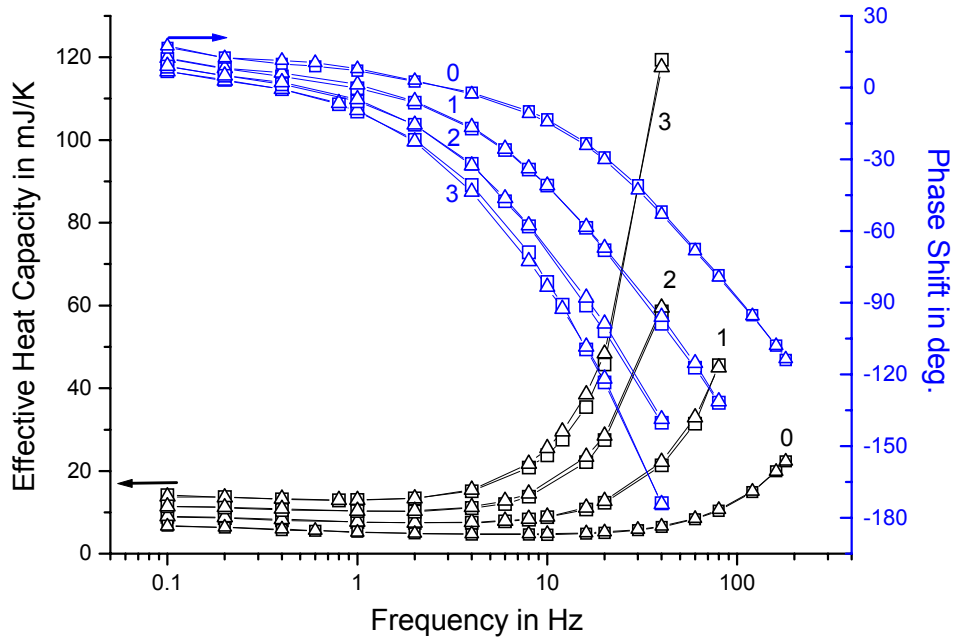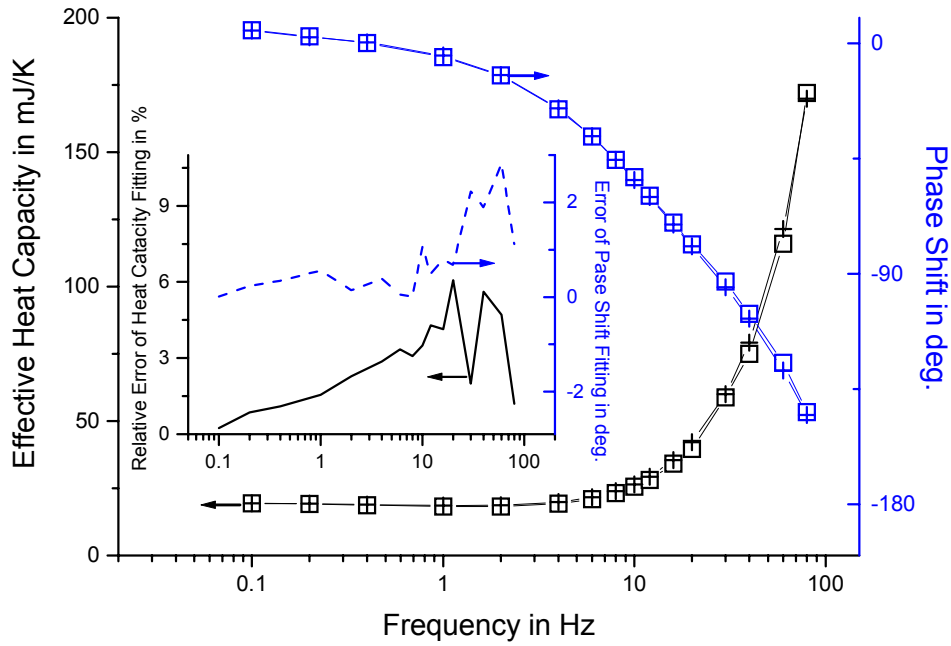

Fig. 5.2. Frequency dependencies of measured (squares) and calculated (triangles) effective heat capacity $C_{eff}(300K)$ and phase shift $\varphi = - Arg(C_{eff})$; 0 – for the empty cell, 1 - for one sapphire sample in the cell, 2 – two identical sapphire samples in the cell and 3 – three samples in the cell. The parameters of the grease layer thickness were as follows: p = 0.95, 1.00, 1.10, 1.01, correspondingly.

Fig. 5.3. Frequency dependencies of measured (squares) and calculated (crosses) effective heat capacity C_{eff}(300K) and phase shift φ = - Arg($\mathbf{C}_{eff}$) for single-crystalline copper disk of diameter 3.1mm and thickness 0.50mm. The curves correspond to the following sample's parameters: c_s = (3.4 ± 0.05)·10^6 J/m^3·K and κ_s = 420 ± 20 W/m·K. The relative error of the effective heat capacity fitting, δC_{eff}, and the absolute error of the phase shift fitting, $\Delta\varphi$, are shown in the insert.

The analogous measurements for a nickel monocrystalline sample were performed. The sample was the roughly polished disk of 3.1 mm diameter and 310 μm thickness. The experimental curves were well described by Eq.(5.4) at the following parameters: C_s=9.1 mJ/K, $\alpha_s/\sqrt{f}$ =0.283 s$^{1/2}$ and p = 1.75. The parameter p was untypical large because of rough surface treatment with 10μm diamond paste. The results correspond to the following sample's thermal parameters: c_s = (3.9 ± 0.08)·10^6 J/m^3·K and κ_s = 29 ± 2 W/m·K. The specific heat capacity is in agreement with the data available in the Web page [5.16]: c = 444 J/kg·K and density ρ = 8900 kg/m^3, i.e. c = 3.95·10^6 J/m^3·K. The thermal conductivity of Ni is dependent on mechanical treatment and purity. As follows from [5.16 - 5.18], the value of κ_s can be in the range 20 – 90 W/m·K.

Finally, consider the possibility of C_s(T) and κ_s(T) measurements at a fixed frequency. In this case, the parameters κ_s and p cannot be determined separately. Assume, that the parameter p is equal to the average value p_0 = 1 within 10% accuracy. Then, the parameters C_s(T) and κ_s(T) can be calculated from the measured C_{eff} at a fixed frequency according to Eq.(5.4) at p = p_0. The uncertainty of the parameter p leads to the error in the measured thermal conductivity. This error depends on the sample's thermal conductivity. The smaller the thermal conductivity κ_s, the smaller the relative error $\delta\kappa_s = \Delta\kappa_s/\kappa_s$ at the same uncertainty of p. The relation between $\delta\kappa_s$ and δp can be find from Eq.(5.4) by fitting C_{eff}(f, $\alpha_s+\delta\alpha_s$, p_0) to C_{eff}(f, α_s, $p_0+\delta p$). The error $\delta\kappa_s$ is related to the error $\delta\alpha_s$. Thus, we find the following relation between $\delta\kappa_s$ and δp at different κ_s: $\delta\kappa_s$ = 2.5% at κ_s = 1 W/m·K, $\delta\kappa_s$ = 5% at κ_s = 10 W/m·K, $\delta\kappa_s$ ca. 100% at κ_s = 500 W/m·K, when δp ca. 10%, and $\delta\kappa_s$ = 30% at κ_s = 500 W/m·K, when δp = 5%. Therefore, the temperature dependencies C_s(T) and κ_s(T) of the materials with κ_s ca. 10 W/m·K can be measured simultaneously at a fixed frequency, provided the uncertainty of the thermal contact conductance is not too large. The approximation of the average thermal contact conductance can not be applied for materials with large thermal conductivity κ_s ca. 500 W/m·K. In this case,

the measurements at different frequencies are impossible.

Thus, the advanced AC calorimetry can be successfully applied for simultaneous measurements of heat capacity and thermal conductivity of various materials with thermal conductivity varied in the broad range, provided the thermal contact conductance on the sample's faces is taken into account. The algorithm how to calculate the sample's thermal properties from the measured effective heat capacity is developed. Thus, the new capabilities of AC calorimetry, when working at frequencies above the classical limit, were demonstrated. The approximation of the ideal thermal contact conductance can be applied only for materials with low thermal conductivity $\kappa_s < 1$ W/m·K. The approximation of the average thermal contact conductance, $p = p_0$, can be applied for materials with intermediate thermal conductivity $\kappa_s \leq 10$ W/m·K. The thermal properties of the materials with high thermal conductivity, κ_s ca. 500 W/m·K, can be obtained from the frequency dependency of the effective heat capacity, measured in the broad frequency range 0.1 - 100Hz. The linearity of the measurements relative to the sample's thickness was proved. The method can be easily generalized for the case of complex sample's thermal parameters, provided the temperature-modulation amplitudes on both sides of the sample are measured.

5.2. Temperature Properties of Raman Crystals for SRS Applications

The recent increase of the research on developing solid state Raman lasers has been observed due to the improvement of the optical quality of non-linear crystals. The density of Raman scattering centers in solids is much higher than that in gas media. This provides higher Raman gain coefficient G and can result in developing of compact, reliable and efficient SRS cells. At the same time the decrease of the Raman cell length from ~1 meter for gases to a few centimetres for crystals and high threshold pump density few 100 MW/cm^2 leads to the problem of heat removal from a small volume. So, the important characteristics that must be considered for developing high power Raman lasers are a thermal conductivity, a thermo-mechanical strength, and a thermal shock parameter of Raman crystals.

The SRS process is characterised by intrinsic Stokes losses. Theoretically the dissipated energy should be about 10% of the pump energy for the first Stokes radiation ($\nu_R \approx 900$ cm^{-1}) with 1064 nm pumping and about 15% with 1320 nm pumping. For a conversion to the second and third Stokes these values should be two or three times higher, correspondingly. These estimations provide the heat value that should be dissipated in the crystal.

The comparison of thermal parameters of some Raman crystals measured by AC calorimetry technique are shown in Table 5.1. One can see that the highest thermal conductivity is observed in a diamond crystal, while this material is too expensive for SRS applications. The recently developed $BaWO_4$ crystal has the thermal conductivity coefficient ($\kappa = 3.0$ W/K·m) close to that in other tungstate and molybdate materials: in $KGd(WO_4)_2$ — $\kappa = 2.8 \div 3$ W/K·m, in $CaWO_4$ — $\kappa = 3.2$ W/K·m, in $CaMoO_4$ — $\kappa = 3.5$ W/K·m. Barium tungstate crystal possesses three times higher κ than barium nitrate which is known as the best material for Raman laser applications. Rutile (TiO_2) and silica (SiO_2) crystals possess higher thermal conductivity but due to large broadening of the SRS mode they have lower Raman gain. The heat capacity value (c) in different solids is presented in the last column (Table 5.1). They are

about $2 \cdot 10^6$ J/K·m^3. Varying from $1.8 \cdot 10^6$ J/K·m^3 for diamond, $3.2 \cdot 10^6$ J/K·m^3 in rutile and $2.1 \cdot 10^6$ J/K·m^3 for BaWO$_4$.

We investigated the temperature dependencies of the heat capacity and thermal conductivity in CaWO$_4$ and BaWO$_4$ crystals (Tables 5.2, 5.3). It was found that they exhibit monotonic functions in the temperature range $100 \div 300$K as follows from the temperature dependencies of the phase and the amplitude of the thermal wave transmitted through the sample (Fig. 5.4, 5.5).

Table 5.1. Thermal conductivity and heat capacity of some nonlinear Raman crystals.

Crystal	v_R, cm^{-1}	Thermal conductivity, W/K·m	Heat Capasity, $10^6 \cdot$ J/K·m^3
Diamond	1332	550*	1.8*
KGd(WO$_4$)$_2$	901	2.8	2.4
	767	3.4	2.4
Ba(NO$_3$)$_2$	1047	1.17*	
NaNO$_3$	1069		2.3*
CaWO$_4$	911	3.2	2.5
BaWO$_4$	924	3.0	2.1
CaMoO$_4$	879	3.5	2.4
SrMoO$_4$	887	3.8	2.6
LiNbO$_3$	250	4.6*	
	632	4.6*	
Y$_3$Al$_5$O$_{12}$	783	13*	2.2*
TiO$_2$	449	8	3.2
SiO$_2$	464	9.5… 6.1*	2.0*

*-literature data

One can see that lowering BaWO$_4$ crystal temperature to 150°K results in the 1.5 times increase of its conductivity from 3.0 W/K·m to 4.3 W/K·m and twice reduction of heat capacity from 2.1·10^6 J/K·m^3 to 1.0·10^6 J/K·m^3. Similar behaviour was observed in CaWO$_4$ crystal with more than twice increase of thermal conductivity and twice reducing heap capacity with cooling the sample to 100 K. These experiments allow to predict that cooling of the Raman crystal can improve its operation as Raman medium due to SRS mode narrowing as well as to improve their thermal properties.

Table 5.2. Thermal conductivity and heat capacity of CaWO$_4$ crystal at 100, 150, 200, 300°K.

Temperature, ^{o}K	Thermal conductivity, W/K·m	Heat Capasity, 10^6 J/K·m^3
100	6.8	1.07
150	4.5	1.6
200	3.8	1.9
300	3.2	2.5

Table 5.3. Thermal conductivity and heat capacity of BaWO$_4$ crystal at 100, 150, 200, 300°K.

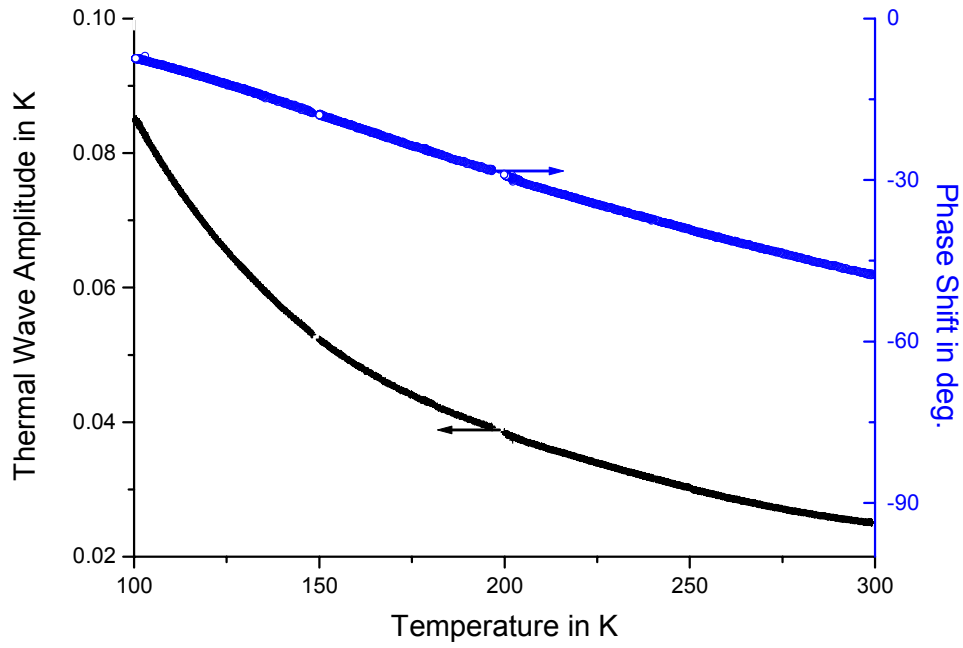| Temperature, ^{o}K	Thermal conductivity, W/K·m	Heat Capasity, 10^6 J/K·m^3
150	4.3	1.0
200	4.0	1.7
300	3.0	2.1

Fig. 5.4. Temperature dependencies of the amplitude and the phase lag of the thermal wave transmitted through the disk-shaped sample (d = 0.49 and ϕ = 3.2) CaWO$_4$ crystal at the modulation frequency 2Hz in AC experiment.
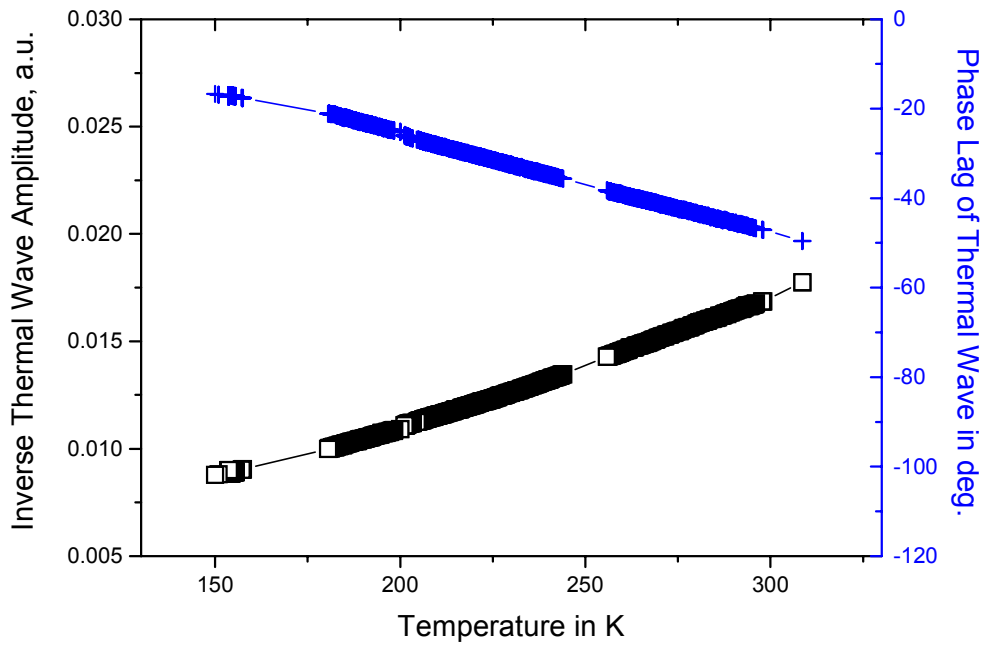

Fig. 5.5. Temperature dependencies of the phase lag (crosses) and the inverse value of the amplitude (squares) of the thermal wave transmitted through the BaWO$_4$ sample at the frequency 2Hz in AC experiment.

5.3. Computer simulations of thermal processes in SRS process

To analyze the influence of the thermal properties on SRS process we made computer simulation of a temperature distribution inside Raman medium after irradiating with the pump laser pulse. We considered the rectangular $3 \times 3 \times 50 mm^3$ sample with variable thermal conductivity $\kappa = 3...10$ $W/K \cdot m$ and heat capacity $c = 2...4 \cdot 10^6 \cdot J/K \cdot m^3$. The sample was heated uniformly along the symmetry axis by laser pulse with duration $\tau = 10^{-7} s$, the "step" cross-section profile of the beam with 1×1 mm^2 dimensions was considered. The absorbed and dissipated energy was $\varepsilon = 1.3$ J. The uniform temperature step was smeared with time according to the following exact solution:

$$T(x,y,t) = (T_0 / 4\pi at) \int_{X_1}^{X_2} \int_{Y_1}^{Y_2} \exp\left[-\frac{(x-\xi)^2 + (y-\eta)^2}{4at} \right] d\xi d\eta$$

here a is the thermal diffusivity which is determined as $a = c/\kappa$. The sample's thermal parameters were assumed to be constant. One can see that the temperature step of 7, 9, and 13 degrees is observed just after the pump pulse in the sample with $c = 4,3,2$ ($\cdot 10^6$ $J/K \cdot m^3$) and are shown in Figs. 5.6, 5.8, 5.9. The relaxation of this temperature shock requires about 100 ms and even longer and depends on the thermal conductivity of the material. Figs. 5.6, 5.7 present results for crystals with thermal conductivity 3 and 10 $W/K \cdot m$. One can see that for higher κ $=10$ $W/K \cdot m$ (Fig. 5.7) the relaxation of the thermal shock is approximately 5 times quicker than for $\kappa = 3$ $W/K \cdot m$ (Fig. 5.6). This strongly influences on the temperature gradient inside the sample.

Fig. 5.10 presents the temperature gradient inside the sample 10 ms after the laser pulse for materials with various thermal parameters. It can be up to 30 K/mm for sample with the poorest thermal properties ($c = 2 \cdot 10^6$ $J/K \cdot m^3$ and $\kappa = 3$ $W/K \cdot m$. The increase of the thermal conductivity coefficient and heat capacity results in the lowering of the temperature gradient in the sample.

Thus, the thermal properties of Raman crystal are very important for high power laser

development and should be considered if one need to develop solid state Raman shifter. The better thermal properties provide lower temperature gradient and correspondingly less thermal beam distortions, self-focusing and mechanical stress inside the element and prevents the damage of the crystal.
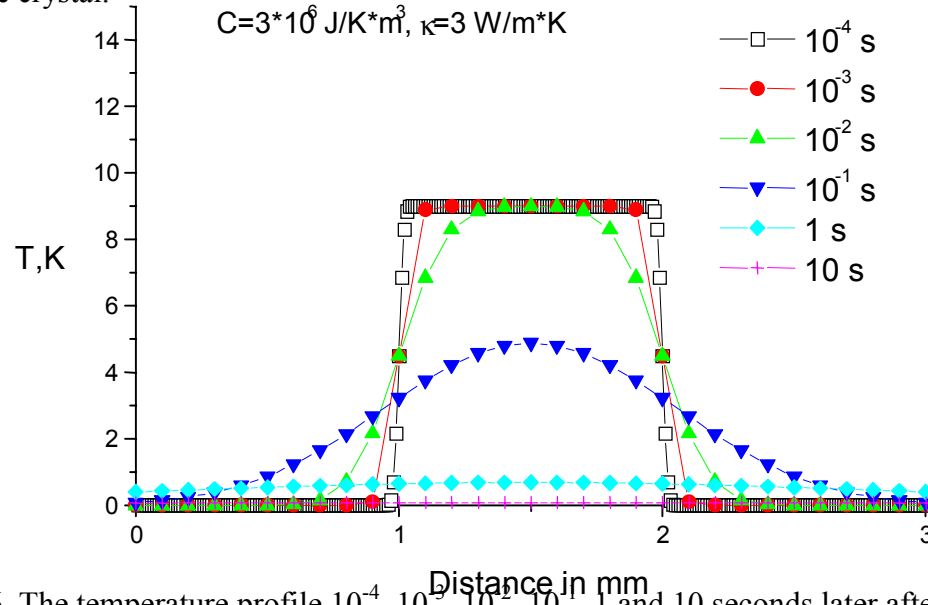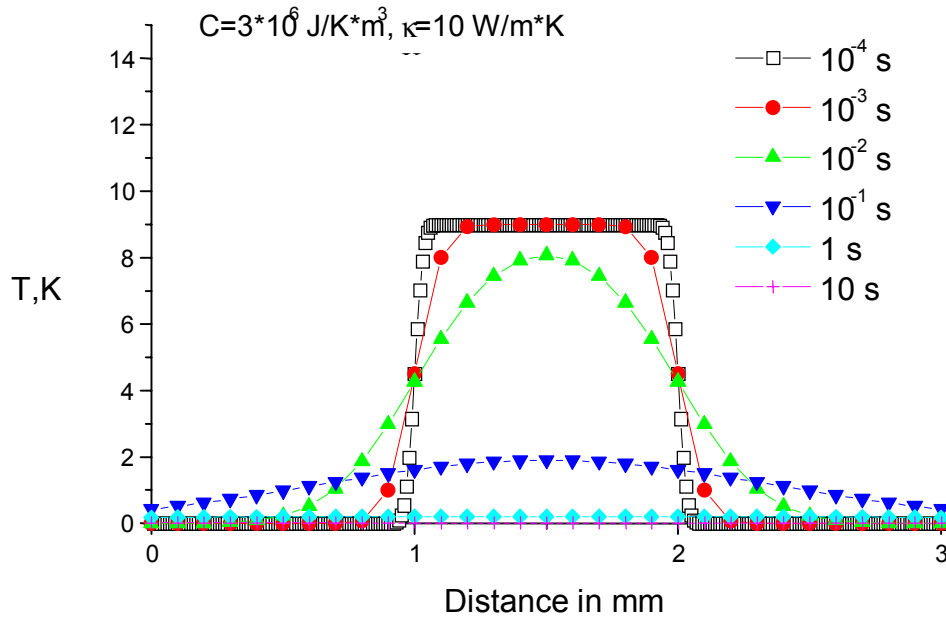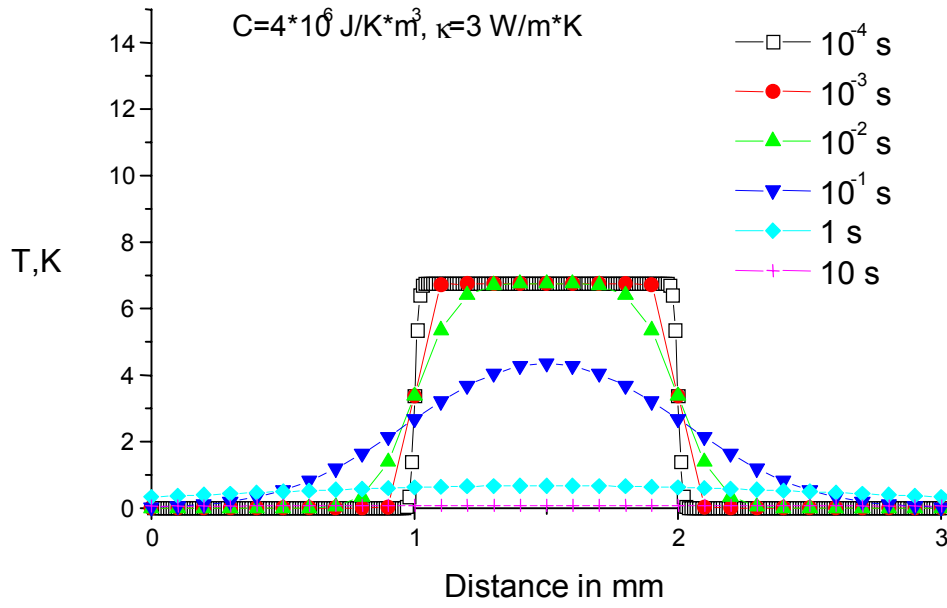

Fig. 5.6. The temperature profile 10^{-4}, 10^{-3}, 10^{-2}, 10^{-1}, 1 and 10 seconds later after pumping pulse irradiation inside the Raman crystal with $c=3 \cdot 10^6$ J/K·m^3 and $\kappa=3$ W/K·m).
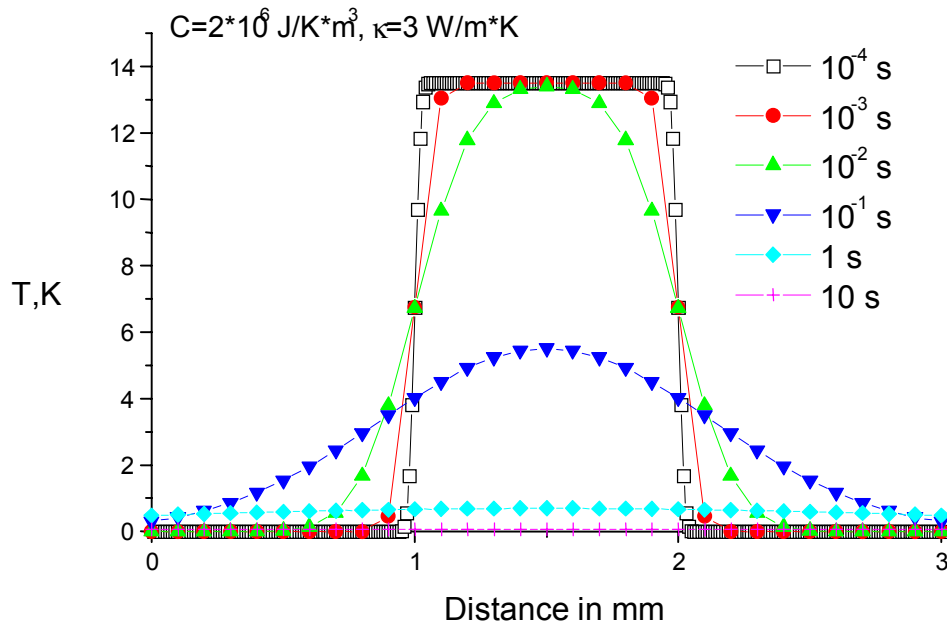

Fig. 5.7. The temperature profile 10^{-4}, 10^{-3}, 10^{-2}, 10^{-1}, 1 and 10 seconds later after pumping pulse irradiation inside the Raman crystal with c=3·10^6 J/K·m^3 and k=10 W/K·m).

Fig. 5.8. The temperature profile 10^{-4}, 10^{-3}, 10^{-2}, 10^{-1}, 1 and 10 seconds later after pumping pulse irradiation inside the Raman crystal with c=4·10^6 J/K·m^3 and k=3 W/K·m.

Fig. 5.9. The temperature profile 10^{-4}, 10^{-3}, 10^{-2}, 10^{-1}, 1 and 10 seconds later after pumping pulse irradiation inside the Raman crystal with c=2·10^6 J/K·m^3 and k=3 W/K·m.
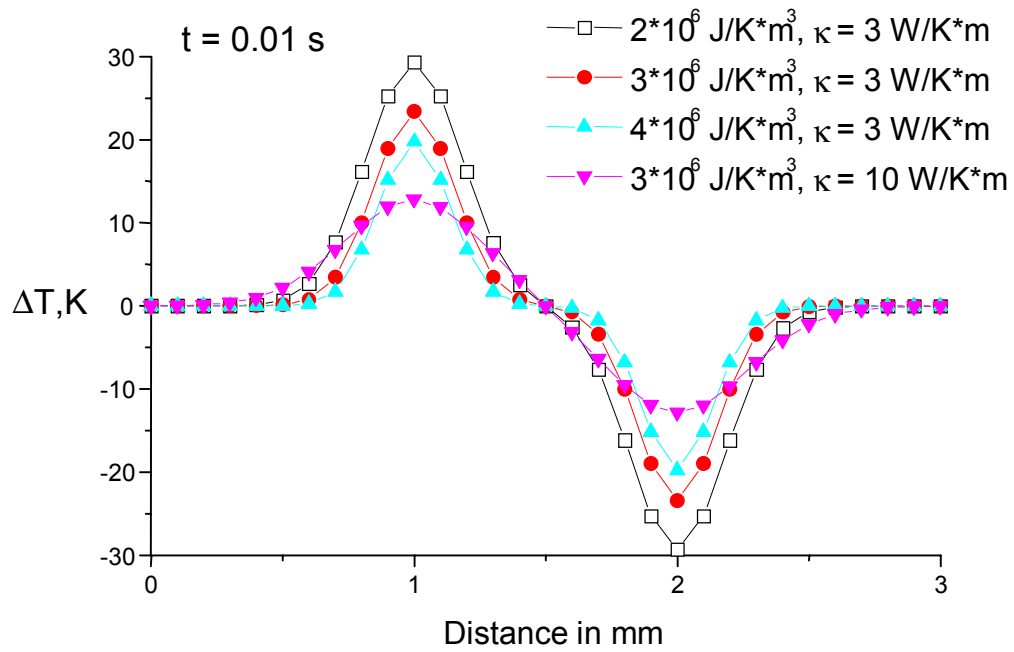
Fig. 5.10. Temperature-gradient inside the sample at t = 0.01s after the laser pulse. The figure illustrates the dependence of the temperature-gradient on the sample's thermal parameters.

References to chapter 5:

5.1.   P.F. Sullivan, G. Seidel, Phys. Rev. **173** (1968) 679.

5.2.   P. Handler, D.E. Mapother, M. Rayl, Phys. Rev. Lett. **19** (1967) 356.

5.3.   M.B. Salamon, Phys. Rev. B **2** (1970) 214.

5.4.   I. Hatta, A. Ikushima, J. Phys. Chem. Solids **34** (1973) 57.

5.5.   I. Hatta, Y. Nagai, T. Nakayama, S. Imaizumi, J. Phys. Soc. Japan, **52** (1983) Suppl. 47.

5.6.   I. Hatta, Y. Nagai, Mol. Cryst. Liq. Cryst. **123** (1985) 295.

5.7.   Ichiro Hatta, Thermochimica Acta **304/305** (1997) 27.

5.8.   K. Ema, H. Yao, Thermochimica Acta **304/305** (1997) 157.

5.9.   Yasuo Saruyama, Thermochimica Acta **304/305** (1997) 171.

5.10. M. Castro, J. A. Puertolas, Thermochimica Acta **304/305** (1997) 291.

5.11. D. Finotello, S. Qian, G. S. Iannacchione, Thermochimica Acta **304/305** (1997) 303.

5.12. A.A. Minakov, Yu.V. Bugoslavsky, C. Schick, Thermochimica Acta **317** (1998) 117.

5.13. A.A. Minakov, C.Schick, Thermochimica Acta, in print

5.14. A.A. Minakov, O.V. Ershov, Cryogenics (ICEC Suppl.) **34** (1994) 461.

5.15. A. A. Minakov, Thermochimica Acta **304/305** (1997) 165.

5.16. Web page Catalogue: http:// www.goodfellow.com

5.17. I. G. Kozhevnikov, L. A. Novitskii, Therm.-Phys. Properties of Materials at Low Tempr., Moscow 1982.

5.18. I. K. Kikoin, Tables of Physical Values, Moscow 1976.

5.19. I. S. Grigoriev, E. Z. Meilikhov, Physical Values, Moscow 1991.